2:1 Clays

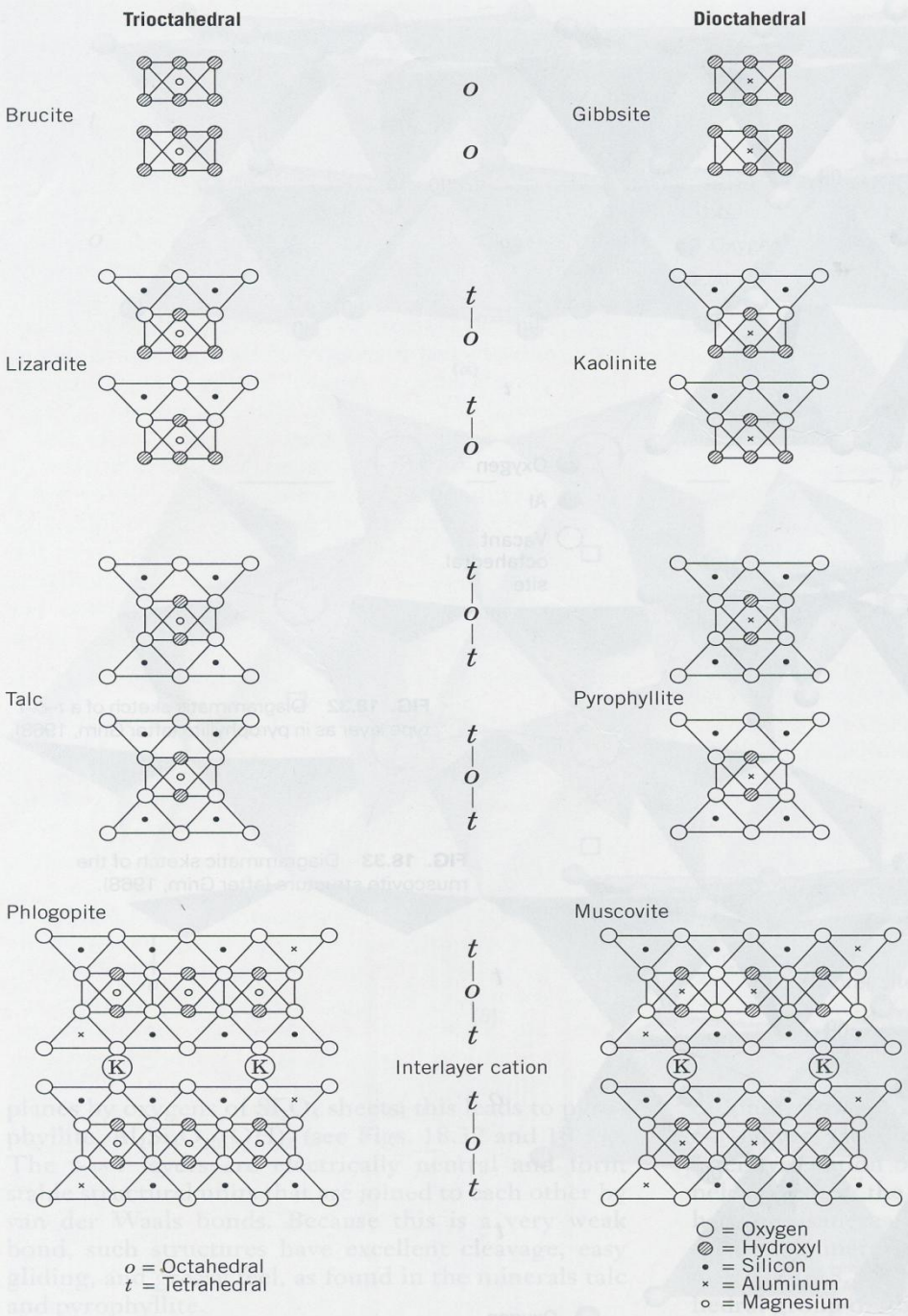
Trioctahedral
Dioctahedral
Brucite
Gibbsite
o
o
Lizardite
Kaolinite
t
o
t
o
Talc
Pyrophyllite
t
o
t
t
o
t
Phlogopite
Muscovite
t
o
t
Interlayer cation
t
o
t
K
K
o = Octahedral
t = Tetrahedral
= Oxygen
= Hydroxyl
= Silicon
= Aluminum
= Magnesium

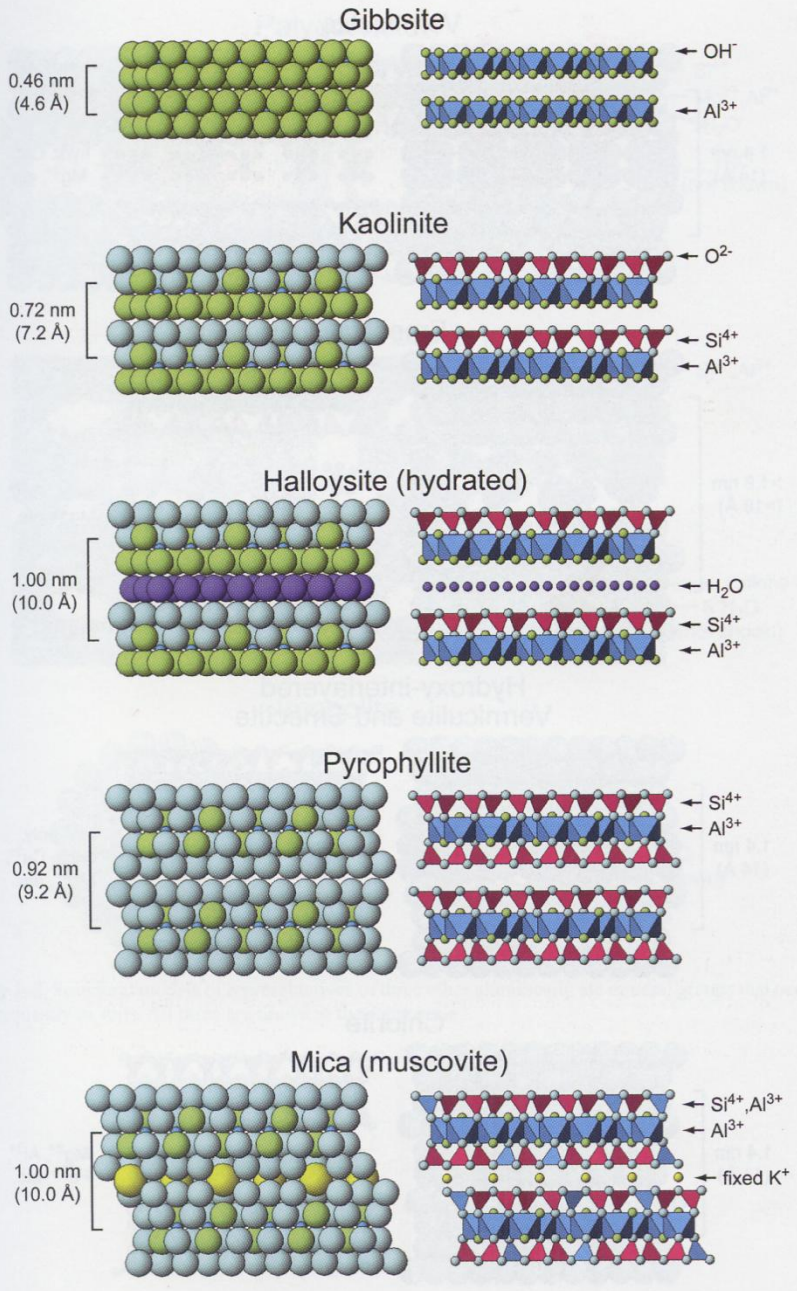

late 1–7. Structural scheme of soil minerals based on octahedral and tetrahedral sheets.

Table 13–1. Theoretical and representative observed formulas for members of the pyrophyllite–talc group.

Mineral and reference†	Ideal formula				Representative observed formula‡			
	Interlayer	Octahedral	Tetrahedral	Anions	Interlayer	Octahedral	Tetrahedral	Anions
					Dioctahedral			
Pyrophyllite (1)	--	Al_2	Si_4	$O_{10}(OH)_2$	$M^{+}_{0.01}$§	$Al_{2.01}Fe^{2+}_{0.01}Mg_{0.02}$	$Si_{3.88}Al_{0.12}$	$O_{10}(OH)_2$
Ferripyrophyllite (2)	--	Fe^{3+}_2	Si^4	$O_{10}(OH)_2$	$M^{+}_{0.10}$	$Fe^{3+}_{1.87}Mg_{0.11}Al_{0.09}$	$Si_{3.80}Fe^{3+}_{0.16}Al_{0.04}$	$O_{10}(OH)_2$
					Trioctahedral			
Talc (1)	--	Mg_3	Si_4	$O_{10}(OH)_2$	$M^{+}_{0.02}$	$Mg_{2.89}M^{3+}_{0.03}M^{2+}_{0.10}$	$Si_{3.97}Al_{0.03}$	$O_{10}(OH)_2$
Willemseite (3)	--	Ni_3	Si_4	$O_{10}(OH)_2$	$M^{+}_{0.04}$	$Ni_{2.11}M^{2+}_{0.80}M^{3+}_{0.10}$	$Si_{3.93}Al_{0.07}$	$O_{10}(OH)_2$
Minnesotaite (3)¶	--	Fe^{2+}_3	Si_4	$O_{10}(OH)_2$	$M^{+}_{0.01}$	$Fe^{2+}_{2.16}M^{2+}_{0.71}M^{3+}_{0.12}$	$Si_{3.93}Al_{0.07}$	$O_{10}(OH)_2$
Kerolite (4)	xH_2O#	Mg_3	Si_4	$O_{10}(OH)_2$	$M^{+}_{0.04}\bullet xH_2O$	$Mg_{2.98}M^{2+}_{0.02}$	$Si_{3.96}Al_{0.04}$	$O_{10}(OH)_2$
Pimelite (4)	xH_2O	Ni_3	Si_4	$O_{10}(OH)_2$	xH_2O	$Ni_{2.90}M^{2+}_{0.10}$	Si_4	$O_{10}(OH)_2$

† References for observed formulas: (1) Koster (1982), (2) Coey et al. (1984), (3) De Waal (1970), and (4) derived from observed formulas in Brindley et al. (1979).
‡ Discrepancy in 22 charge basis of observed formulas for pyrophyllite, talc, willemseite, and minnesotaite maybe due to rounding errors or presence of impurities.
§ M = metal cation of valency given.
¶ Minnesotaite is included here but may be placed more appropriately with modulated layer structures (Martin et al., 1991).
# Location of H_2O in all kerolite and pimelite structures is likely on external surfaces as well as within interlayer. x = value ranging from 0.8 to 1.2 (Brindley et al., 1979).

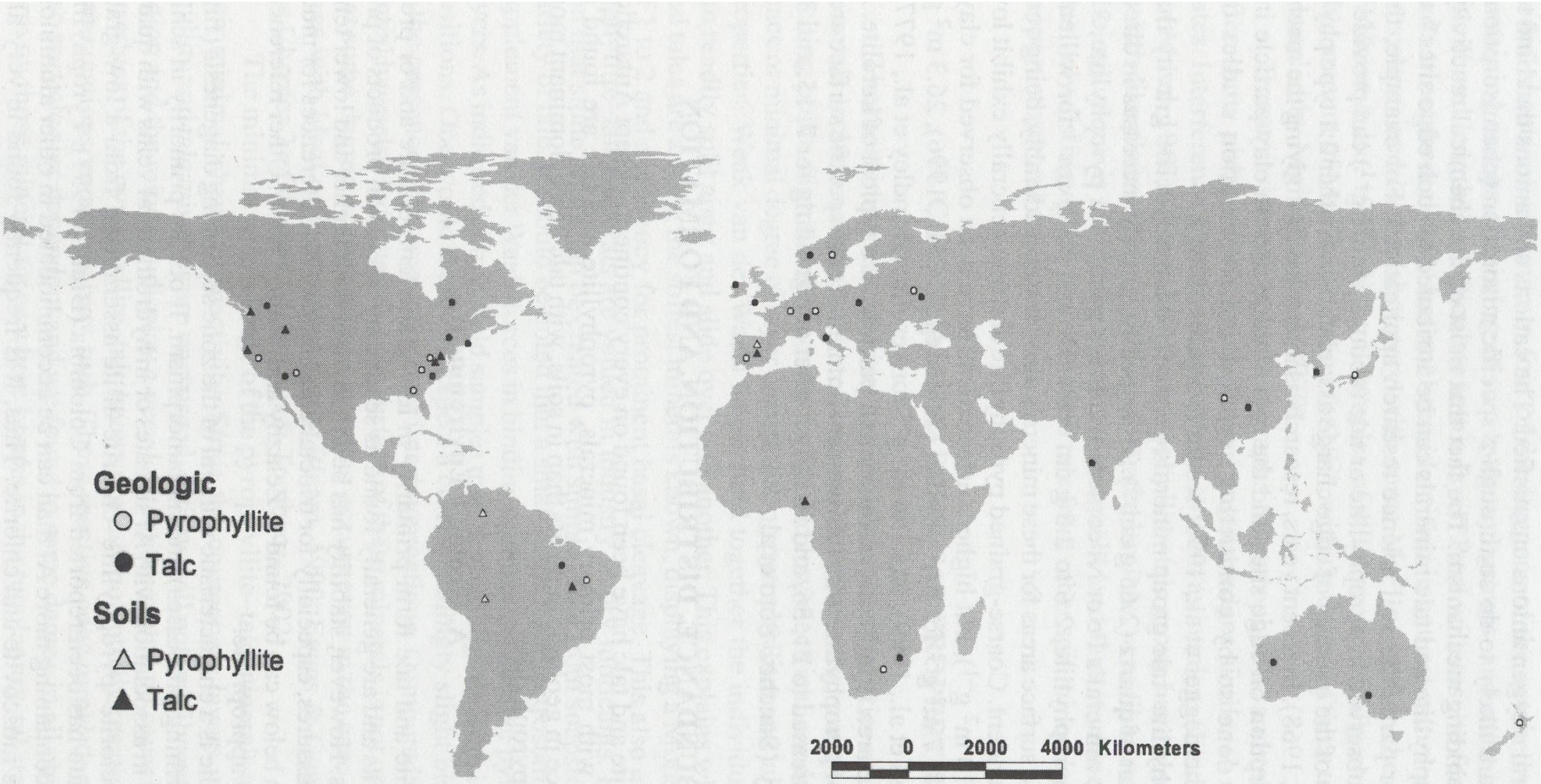

Fig. 13–1. Worldwide distribution of reported pyrophyllite and talc in geologic and soil settings.

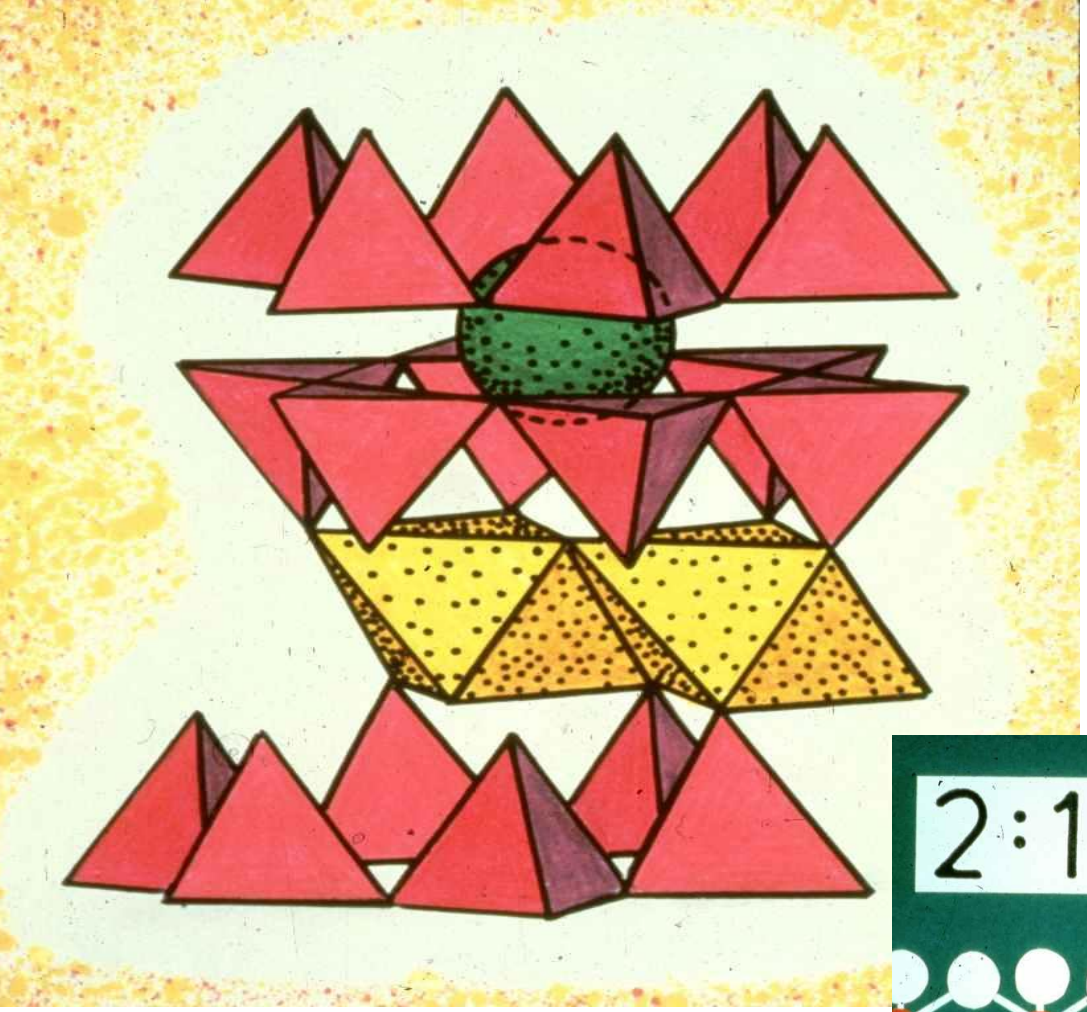

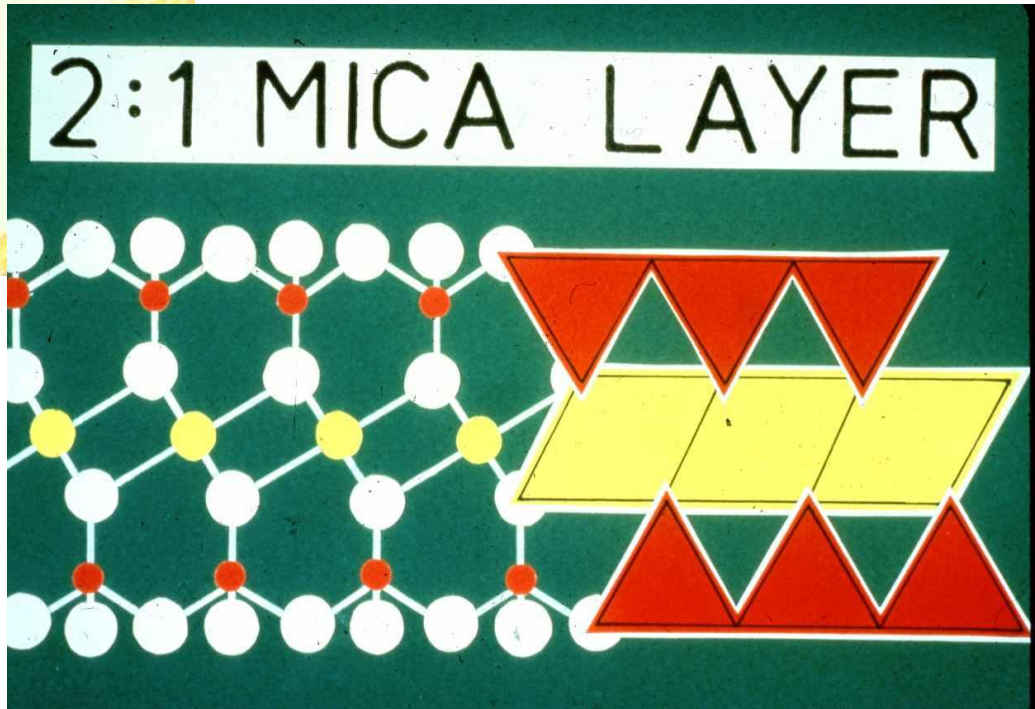
2:1 MICA LAYER

Table 14–1. Idealized chemical formulas and sheet compositions for some trioctahedral and dioctahedral micas.†

Mineral	Cations			Anions	Layer charge
	Tetrahedral sheet composition	Octahedral sheet composition	Interlayer cation		
					mol per formula unit
		Trioctahedral			
Phlogopite	Si_3Al	Mg_3	K	$O_{10}(OH)_2$	1
Biotite	Si_3Al	$Mg_{0.6\text{-}1.8}Fe(II)_{2.4\text{-}1.2}$	K	$O_{10}(OH)_2$	1
Annite	Si_3Al	$Fe(II)_3$	K	$O_{10}(OH)_2$	1
Lepidolite	Si_3Al	$[Li,Al]_3$	K	$O_{10}(OH, F)_2$	1
Clintonite	$SiAl_3$	Mg_2Al	Ca	$O_{10}(OH)_2$	2
		Dioctahedral			
Paragonite	Si_3Al	Al_2	Na	$O_{10}(OH)_2$	1
Muscovite	Si_3Al	Al_2	K	$O_{10}(OH)_2$	1
Phengite	$Si_{3.5}Al_{0.5}$	$Al_{1.5}[MgFe(II)]_{0.5}$	K	$O_{10}(OH)_2$	1
Illite	$Si_{3.5}Al_{0.5}$	$Al_{1.75}[MgFe(II)]_{0.25}$	$K_{0.75}$	$O_{10}(OH)_2$	0.75
Glauconite	$Si_{3.67}Al_{0.33}$	$[AlFe(III)]_{1.33}[MgFe(II)]_{0.67}$	K	$O_{10}(OH)_2$	0.8
Margarite	Si_2Al_2	Al_2	Ca	$O_{10}(OH)_2$	2

† Adapted from Bailey (1984).

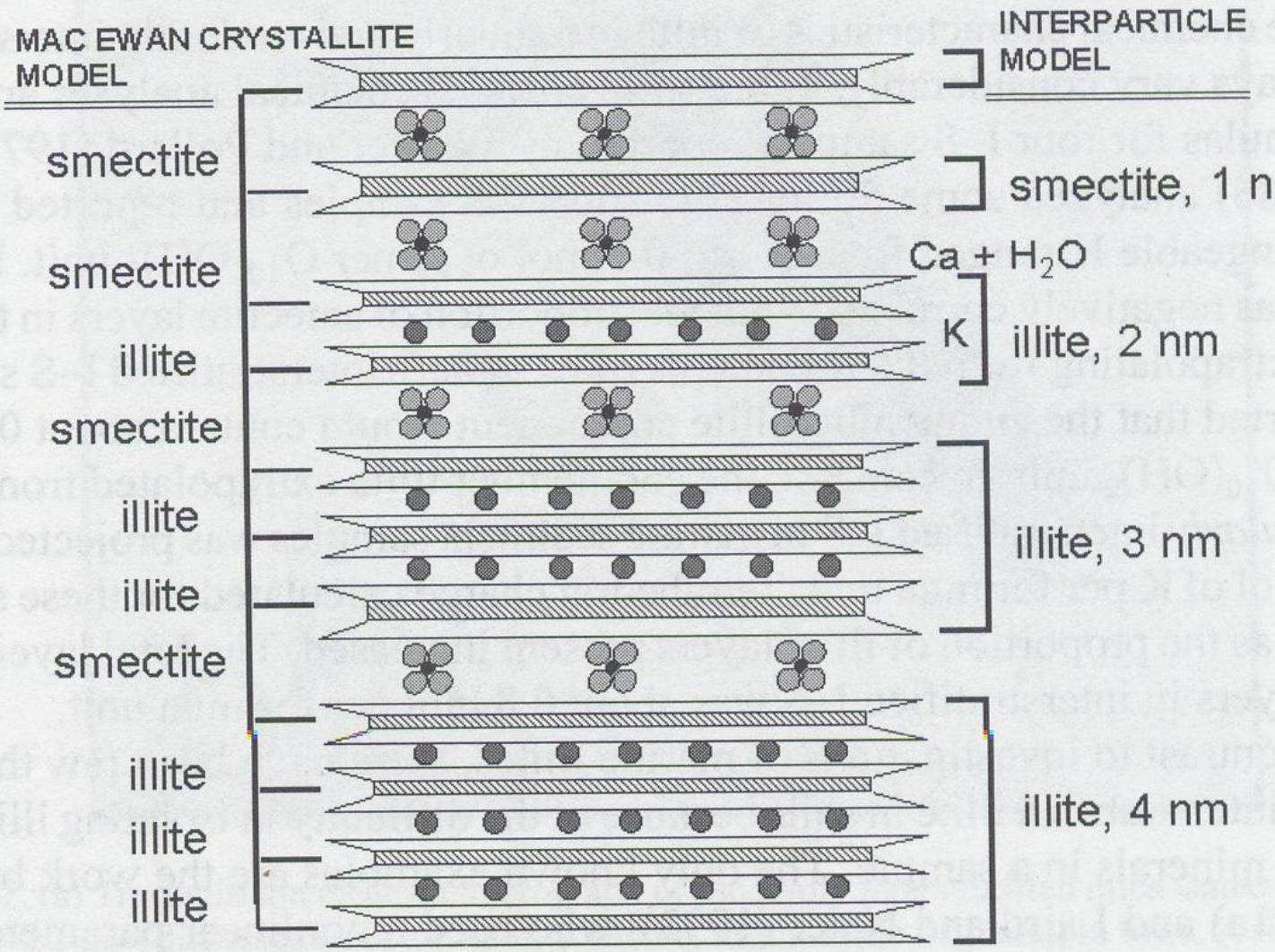

Fig. 14–1. Interstratified illite–smectite can be conceptualized as single crystallites (MacEwan model) or as collections of fundamental particles. High-charge layers are intercalated with K^+ ions (dark circles). Low-charge layers are intercalated with Ca^{2+} and H_2O molecules. In this diagram, smectite appears to be more abundant when the structure is modeled as a single crystallite. Adapted from Nadeau and Bain (1986) and Ahn and Peacor (1986). Not to scale.

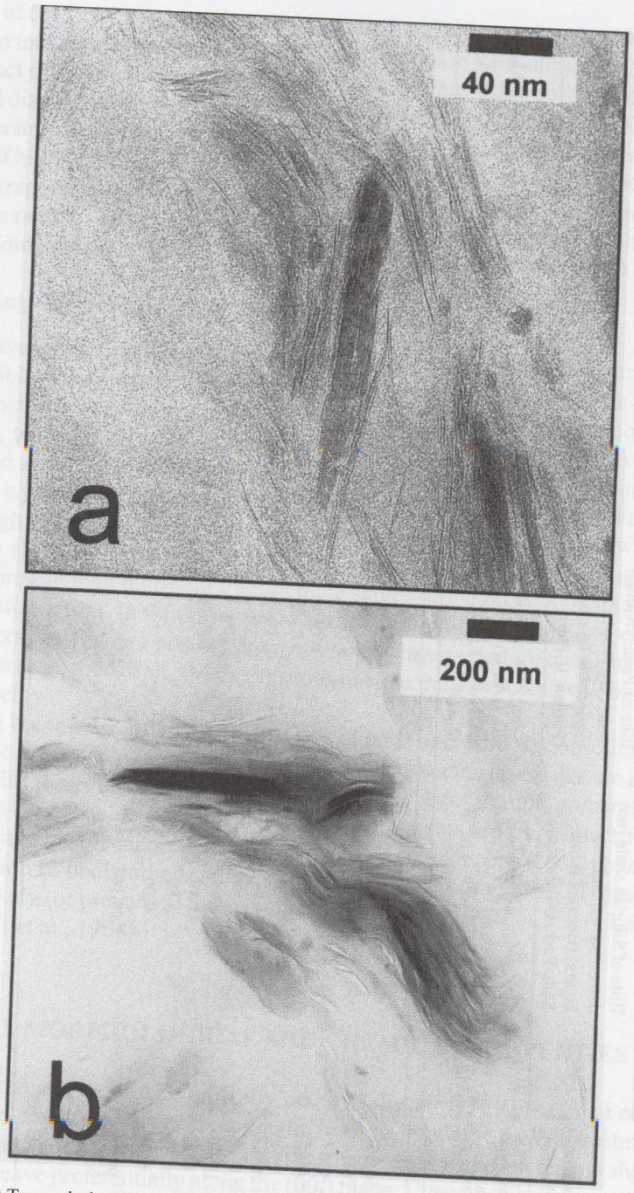

Fig. 14–2. (a) Transmission electron micrograph of randomly interstratified mica–smectite in the fine clay (<0.2 μm) dispersed from a fine-silty, mixed, mesic Typic Argiudoll in Iowa. A rigid core of 1-nm mica layers is surrounded by thin, flexible layers interpreted to be smectitic. (b) Transmission electron micrograph of illite clay particle dispersed from a fine, smectitic, Quaternary paleosol in Iowa (Woida & Thompson, 1993). Note frayed edges where monovalent cations such as K, Cs, or ammonium might be fixed. These samples were ultrasonically dispersed, equilibrated at 0.32 kPa, dehydrated with methanol, and impregnated with Spurr resin (Stucki & Tessier, 1991).

Table 14–2. Chemical analyses and structural formulas† of illites and interstratified illite–smectites. Note that (i) the K_2O content of interstratified illite–smectite decreases with increasing proportions of expandable layers, and (ii) chemical analyses of the shale and underclay samples include H_2O, whereas the analyses of Laird et al. (1991a) were normalized to a water-free basis.

	Illite of Precambrian shale (Montana)‡	Illite of Silurian shale (no detectable expandable layers) (Beavers Bend State Park, Oklahoma)§	Illite of Pennsylvanian underclay (10–15% expandable layers) (Fithian, IL)¶	Illite of Pennsylvanian shale (Petersburg, IL)¶	Illitic phase of interstratified smectite–illite (Webster soil, Minnesota)#
	$Ca_{0.09}Na_{0.02}K_{0.89}$ $(Si_{3.43}Al_{0.57})$ $(Al_{1.51}Fe^{3+}_{0.03}Fe^{2+}_{0.03}Mg_{0.43})$ $O_{10}(OH)_2$	$Ca_{0.02}Mg_{0.06}Na_{0.05}K_{0.59}$ $(Si_{3.47}Al_{0.53})$ $(Al_{1.41}Fe^{3+}_{0.35}Fe^{2+}_{0.11}Mg_{0.13})$ $O_{10}(OH)_2$	$Ca_{0.02}Mg_{0.13}Na_{0.02}K_{0.52}$ $(Si_{3.45}Al_{0.55})$ $(Al_{1.51}Fe^{3+}_{0.23}Fe^{2+}_{0.10}Mg_{0.16})$ $O_{10}(OH)_2$	$Ca_{0.02}Mg_{0.24}Na_{0.01}K_{0.43}$ $(Si_{3.11}Al_{0.89})$ $(Al_{1.34}Fe^{3+}_{0.64}Fe^{2+}_{0.00}Mg_{0.02})$ $O_{10}(OH)_2$	$Ca_{0.12}K_{0.23}$ $(Si_{3.61}Al_{0.39})$ $(Al_{1.55}Fe^{3+}_{0.26}Mg_{0.23})$ $O_{10}(OH)_2$
	%				
SiO_2	50.55	49.85	51.22	44.01	59.12
Al_2O_3	26.14	23.68	25.91	26.81	26.91
Fe_2O_3	0.67	6.60	4.59	11.99	5.66
FeO	0.65	1.87	1.70	0.00	--
MgO	4.25	1.86	2.84	2.43	2.55
CaO	0.60	0.12	0.16	0.11	1.84
Na_2O	0.19	0.34	0.17	0.07	--
K_2O	10.29	6.64	6.09	4.78	3.01
TiO_2	0.42	1.40	0.53	0.64	0.86
H_2O^+	4.59	6.80	7.14	8.08	--
H_2O^-	0.99	0.00	1.45	2.33	--
Total	99.34	99.16	101.80	101.25	99.95
Total layer charge, mol per $O_{10}(OH)_2$ unit	1.03	0.77	0.81	0.91	0.47

† Assume that TiO_2 is present as rutile or anatase.
‡ Weaver and Pollard (1973).
§ Mankin and Dodd (1963).
¶ Grim et al. (1937).
# Laird et al. (1991a).

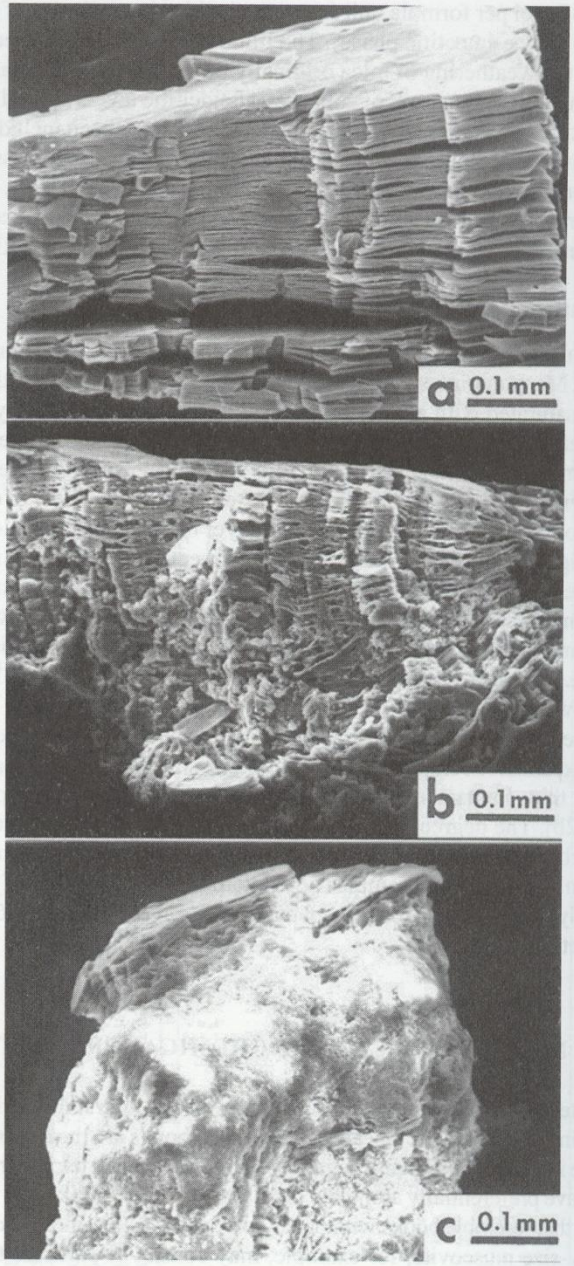

Fig. 14–3. Scanning electron micrographs that illustrate stages of biotite weathering in the saprolite of a North Carolina Hapludult (Graham et al., 1989a). (a) Partially expanded biotite grain (185-cm depth). (b) Expanded and extensively altered biotite grain (120-cm depth). (c) Micaceous morphology is almost completely lost in alteration to secondary minerals (120-cm depth). Presented by permission of The Clay Minerals Society.

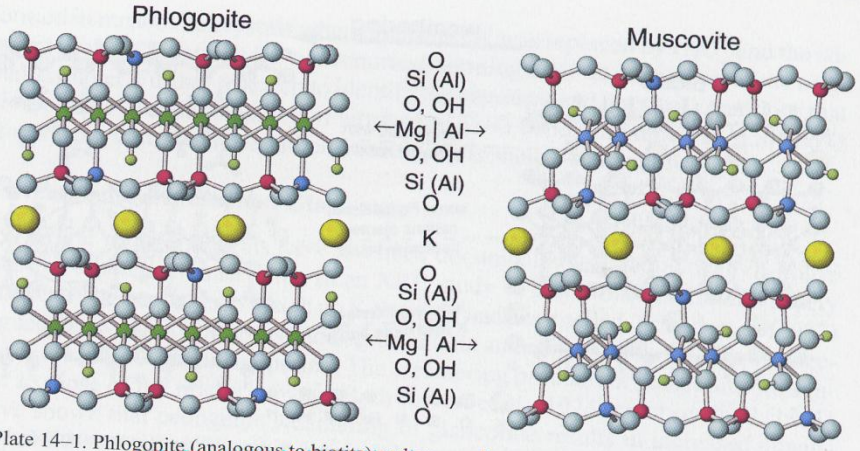

Plate 14–1. Phlogopite (analogous to biotite) and muscovite crystalline structures. Note that the position of the hydroxyl dipole in phlogopite is oriented perpendicularly to the (001) plane because all the octahedral positions are filled with divalent cations. In muscovite, the hydroxyl dipole is tilted toward the empty octahedral position and away from the interlayer K atoms. These structures were derived from neutron diffraction data of Joswig (1972) and Rothbauer (1971).

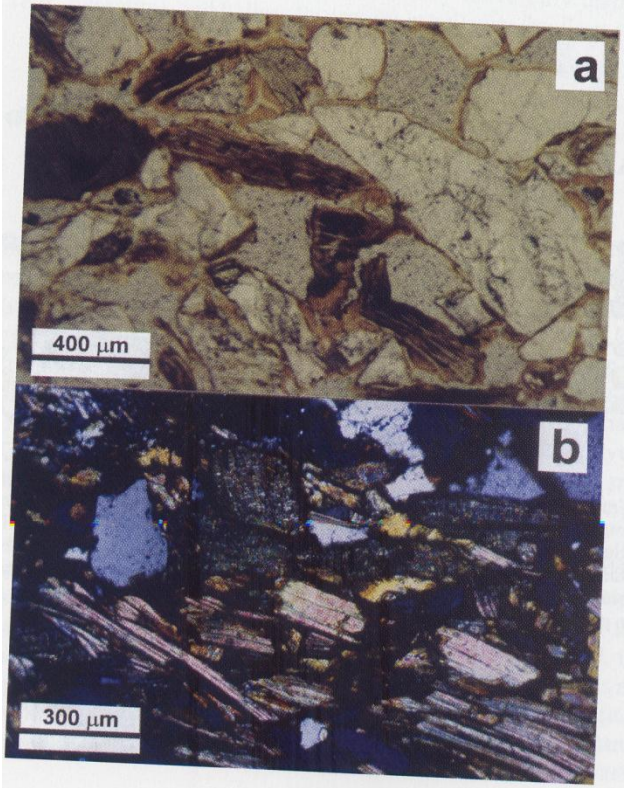

Plate 14–2. Light micrographs of biotite weathering in soil. (a) Exfoliated, weathered biotite pseudomorphs (now vermiculite) in a Natric Palexeralf derived from intrusive igneous rocks in California (plane-polarized light; Nettleton et al., 1968). (b) Parallel, linear alteration of biotite grains in a Typic Hapludult formed in saprolite that was derived from micaceous gneiss in the Virginia Piedmont, USA (cross-polarized light; Stolt et al., 1991).

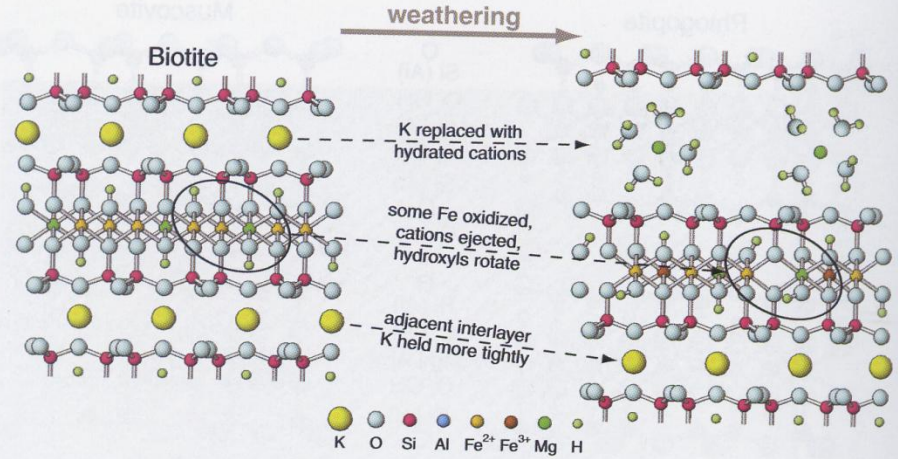

Plate 14–3. Weathering of biotite. In this trioctahedral mineral, hydroxyl dipoles in the octahedral sheet are perpendicular to the basal plane and relatively close to interlayer K ions. In an acidic, oxidizing environment where there is an external sink for K, loss of K and ejection of Fe from one layer cause K in the adjacent layer to be held more tightly as hydroxyls reorient toward the empty octahedral site and away from the remaining interlayer K.

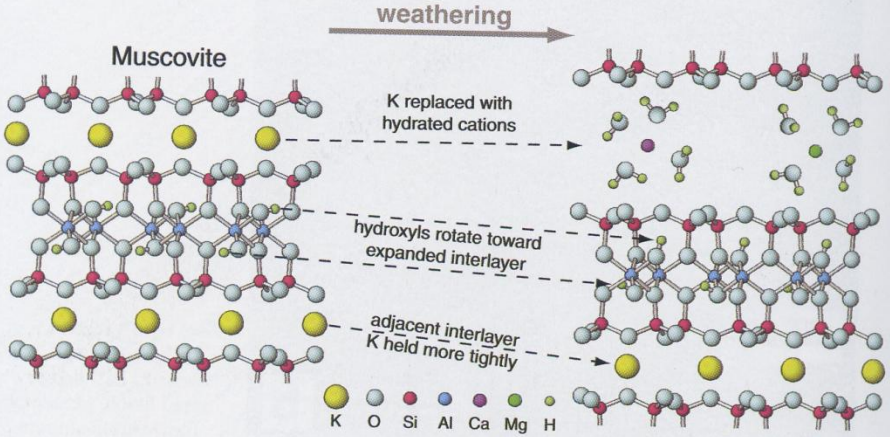

Plate 14–4. Weathering of muscovite. As K is lost from muscovite, positively charged hydroxyl dipoles in the octahedral sheet rotate toward the K-depleted interlayer region (from an angle of 15 to 20° from the horizontal to an angle of 50 to 60° from the horizontal). In this way, K atoms in the remaining, adjacent interlayer are farther from hydroxyl units than they were in the original structure, and they are therefore more resistant to subsequent removal. The expanded portion of the structure may appear in x-ray diffraction patterns to be smectite, as suggested in Fig. 14–1.

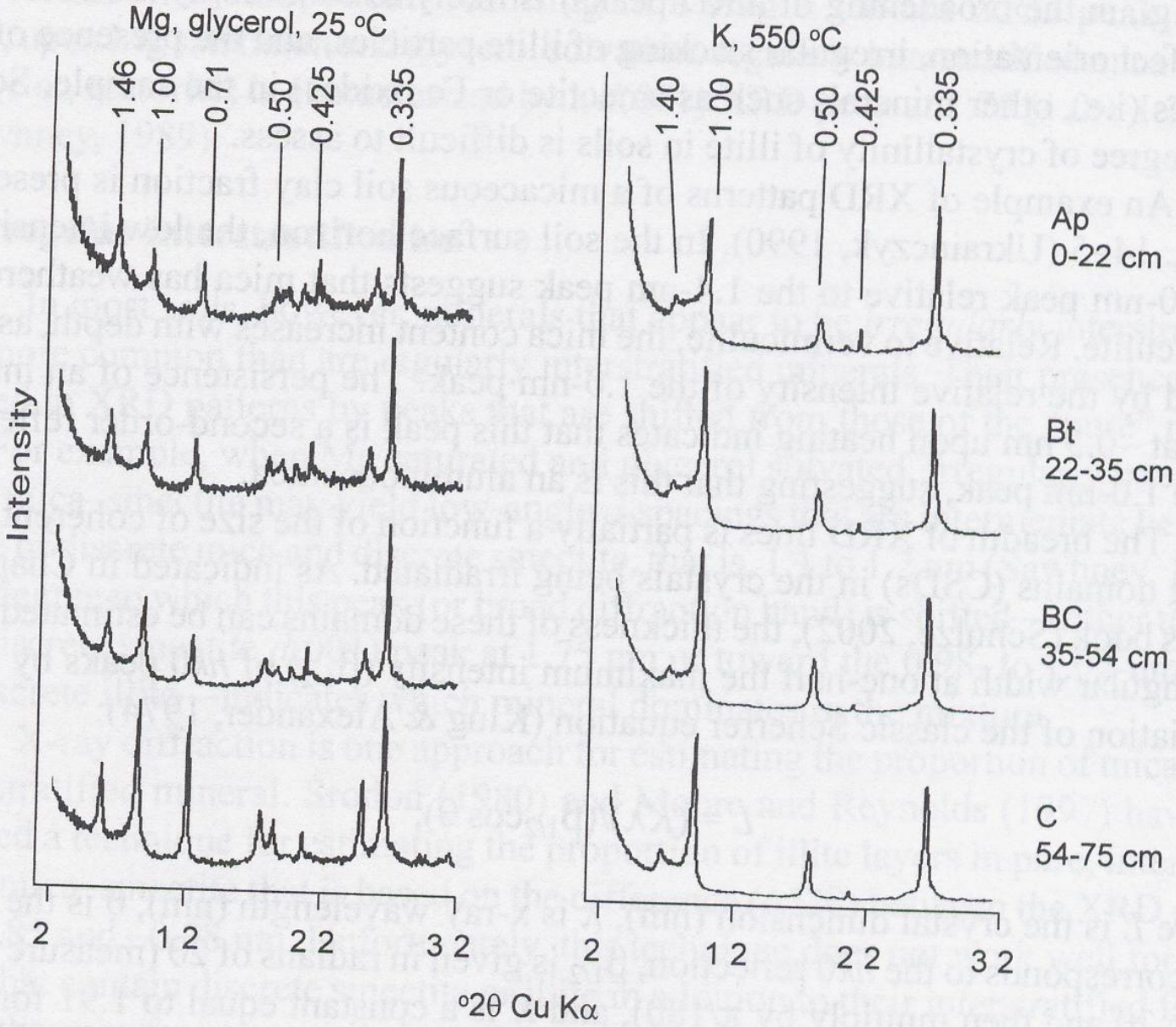

Fig. 14–5. X-ray diffraction patterns of the <2-μm fraction of a Glossoboric Hapludalf in New York (Ukrainczyk, 1990). Note the increase in intensity and sharpness of the 1.0-nm clay mica peak as depth increases.

2. Ion hydration

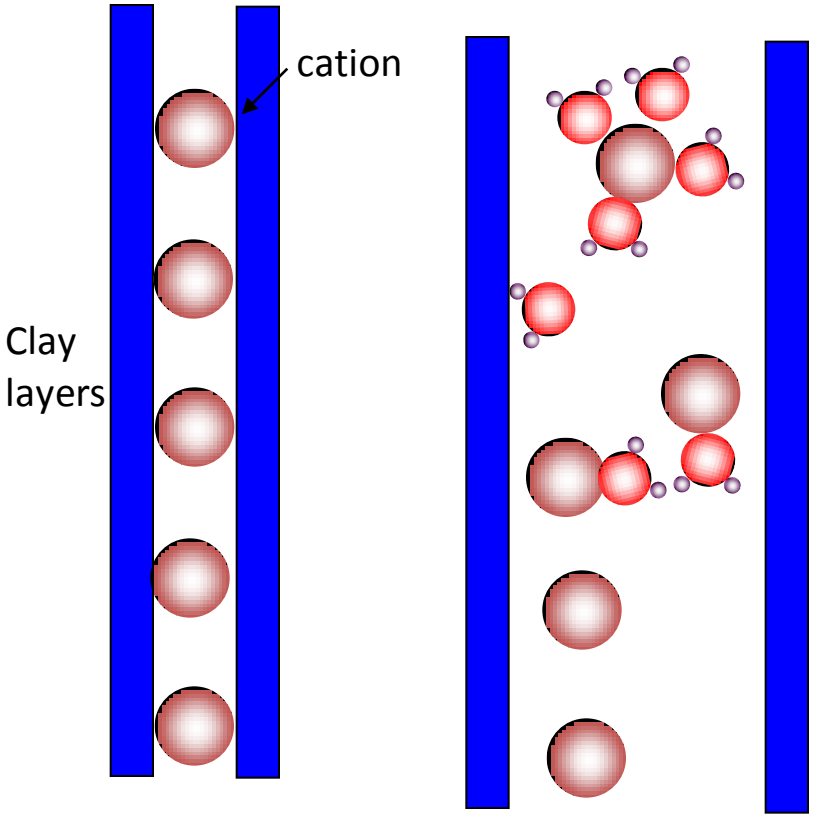

Dry condition

(Interlayer)

The water molecules wedge into the interlayer after adding water

Na^+ crystal radius: 0.095 nm

radius of hydrated ion: 0.358 nm

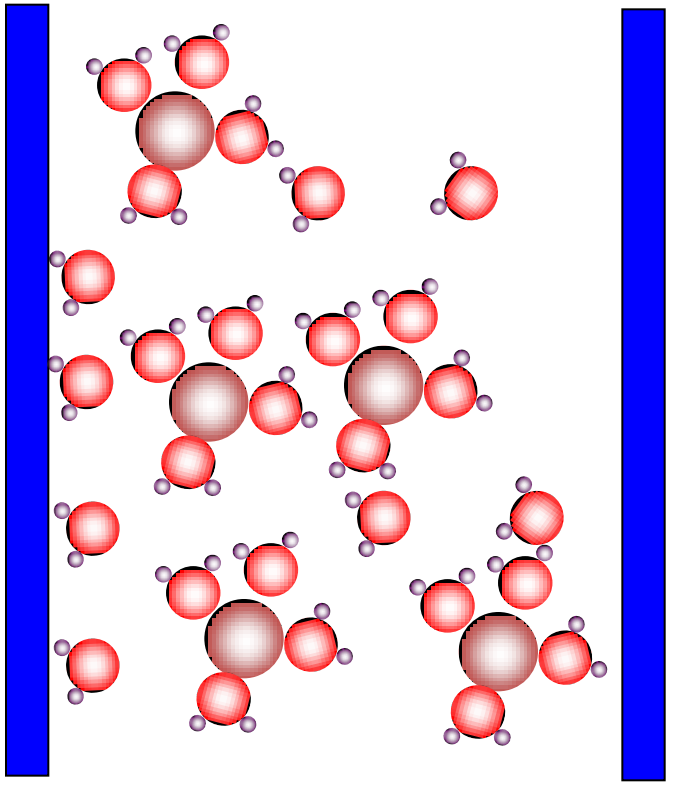

The cations are fully hydrated, which results in repulsive forces and expanding clay layers (hydration energy).

Smectites

Table 15–1. Ideal endmember formulas for minerals in the smectite group.†

Substitution	Dioctahedral	Trioctahedral
Octahedral	Montmorillonite $M^{+}_{0.33}(Si_4)^{IV}(Al_{1.67}Mg_{0.33})^{VI}O_{10}(OH)_2$	Hectorite $M^{+}_{0.33}(Si_4)^{IV}(Mg_{2.67}Li_{0.33})^{VI}O_{10}(OH)_2$
Tetrahedral	Beidellite $M^{+}_{0.33}(Si_{3.67}Al_{0.33})^{IV}(Al_2)^{VI}O_{10}(OH)_2$	Saponite $M^{+}_{0.33}(Si_{3.67}Al_{0.33})^{IV}(Mg_3)^{VI}O_{10}(OH)_2$
	Nontronite $M^{+}_{0.33}(Si_{3.67}Al_{0.33})^{IV}(Fe_3+)_2{}^{IV}O_{10}(OH)_2$	Sauconite $M^{+}_{0.33}(Si_{3.35}Al_{0.65})^{IV}(Zn_3)^{VI}O_{10}(OH)_2$

† *M* represents one or more exchangeable metal cations, and may have a value ranging from 0.2 to 0.6.

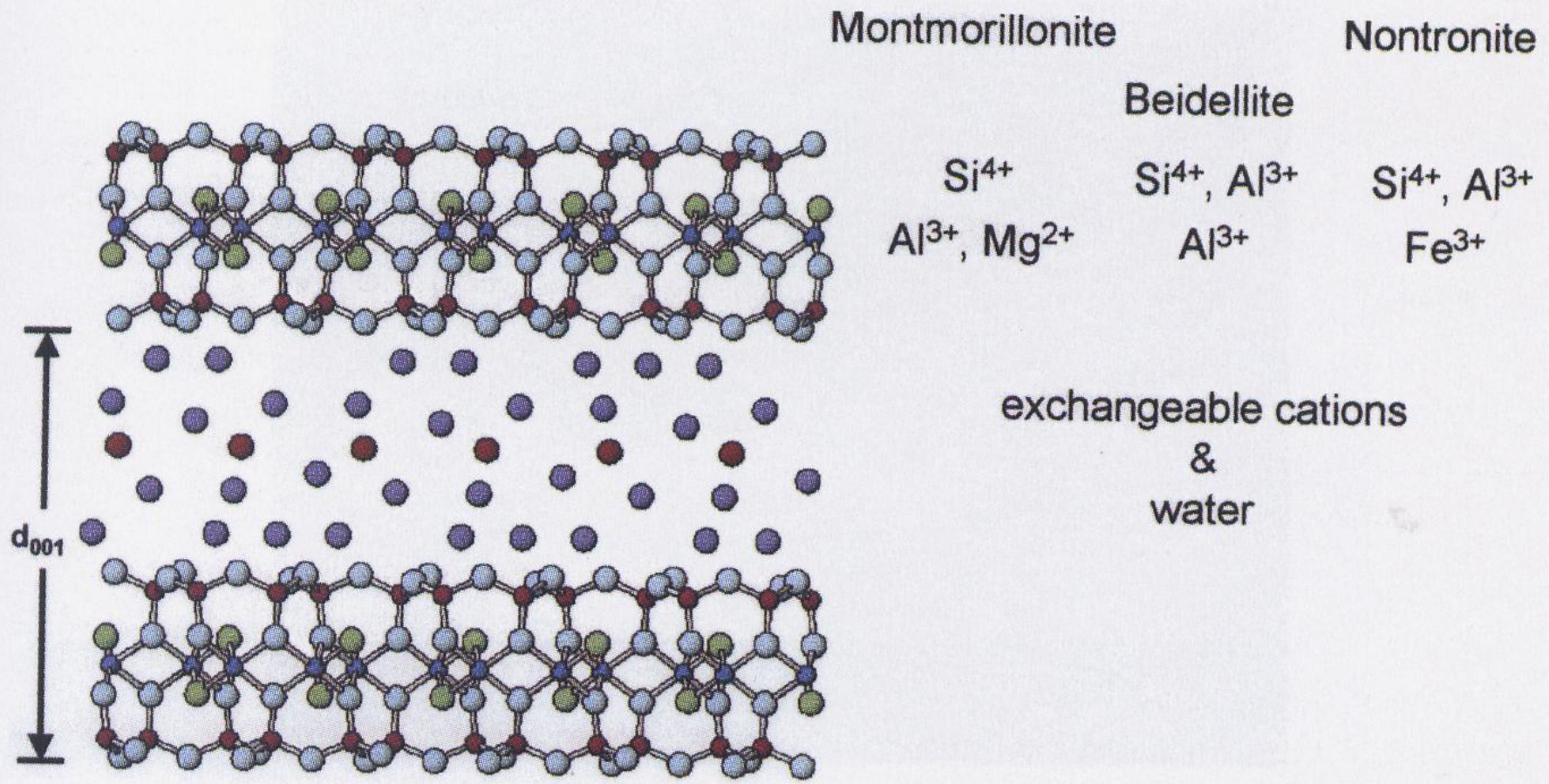

Plate 15–1. Generalized molecular structure of a smectite mineral. Two tetrahedral sheets and one octahedral sheet comprise the 2:1 layer. The interlayer region is shown with Na^{+} ions surrounded by water molecules but more commonly hydrated Ca^{+2} and Mg^{+2} ions occupy this region. The d_{001} spacing shown in this Na-saturated mineral is 1.6 nm. (Figure by G. N. White, College Station, TX).

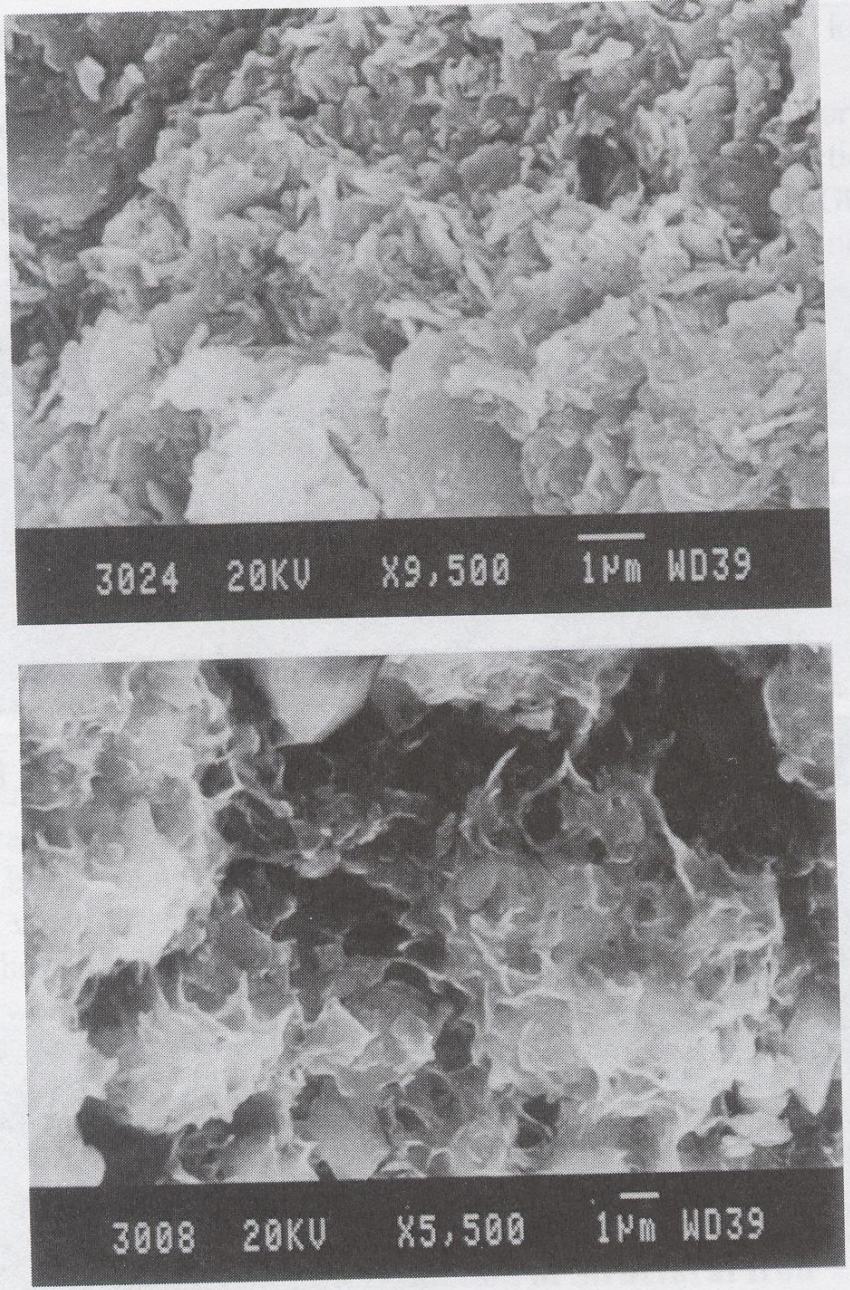

Fig 15–1. Scanning electron micrographs showing cabbage-like structure of neoformed nontronite coated by irregular and larger flakes on the same mineral sample. Magnification is on the photos. (Wiewiora et al., 1996; reprinted with the permission of the Clay Minerals Society, Boulder, CO.).

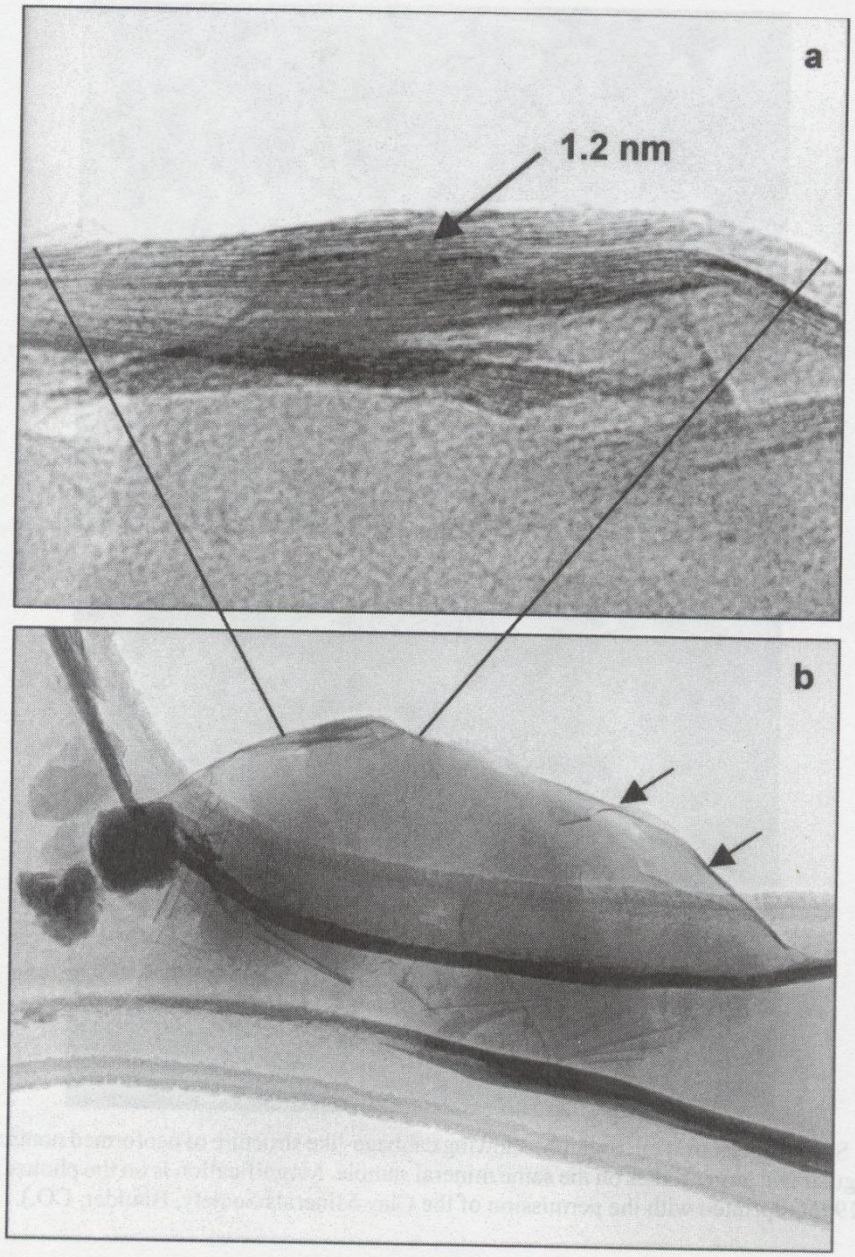

Fig. 15–2. Transmission electron micrographs illustrating characteristic morphologic properties of montmorillonite. (a) The sheet is so thin that only about 10 layers are indicated by the lattice fringes, shown by the fold at the edge of the particle magnified. (b) These layers have a spacing of about 1.2 nm and other folded edges are indicated by the arrows (courtesy of J.B. Dixon).

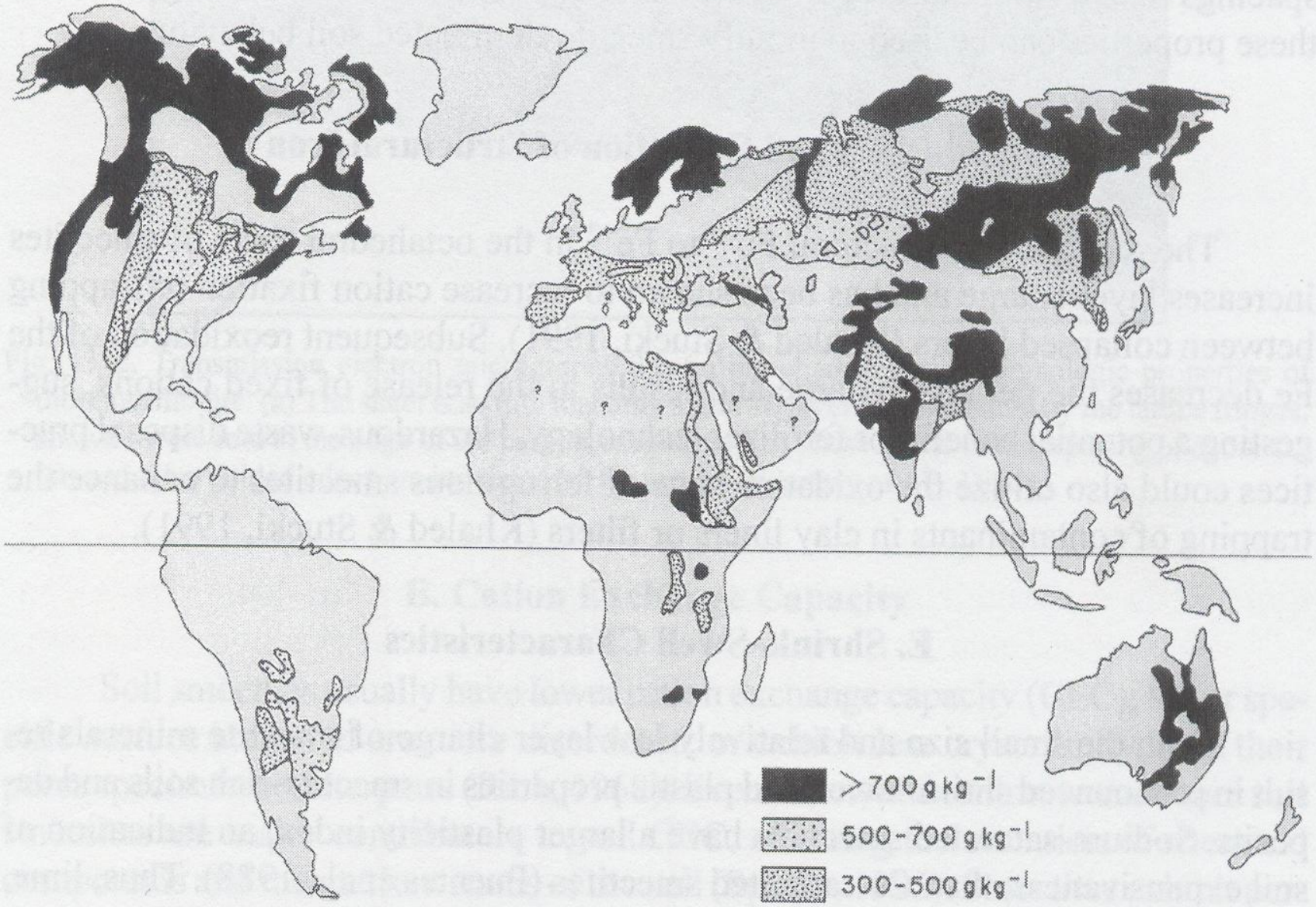

Fig. 15–3. Map of the world showing areas of soil with different proportions of smectite in clay fractions of their surface horizons (from Bordchardt, 1989).

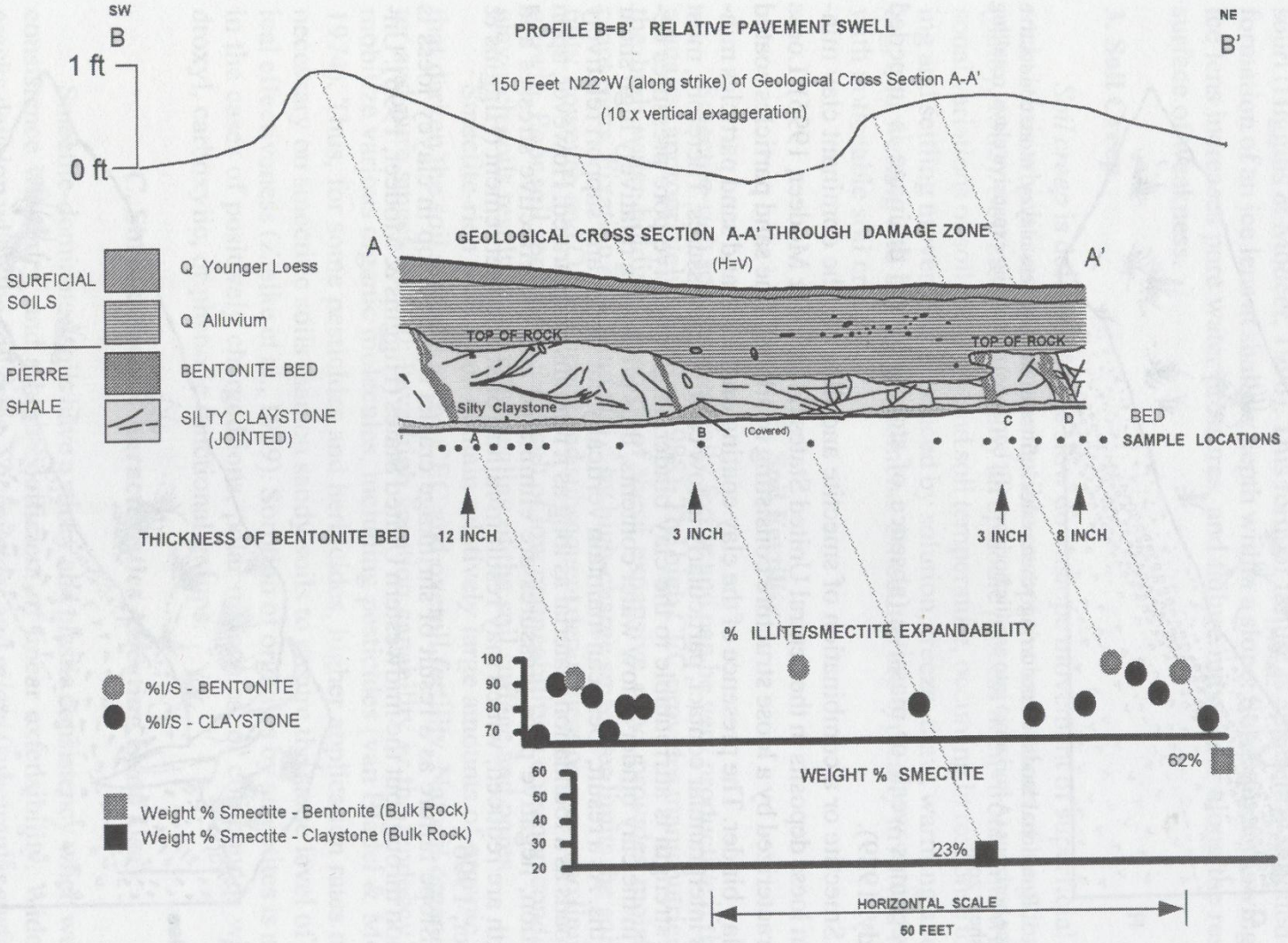

Fig. 15–4. Correlation of pavement damage with bentonite beds and respective percentage I–S and weight percentage of smectite (Gill et al., 1996; reprinted with the permission of the Clay Minerals Society, Boulder, CO).

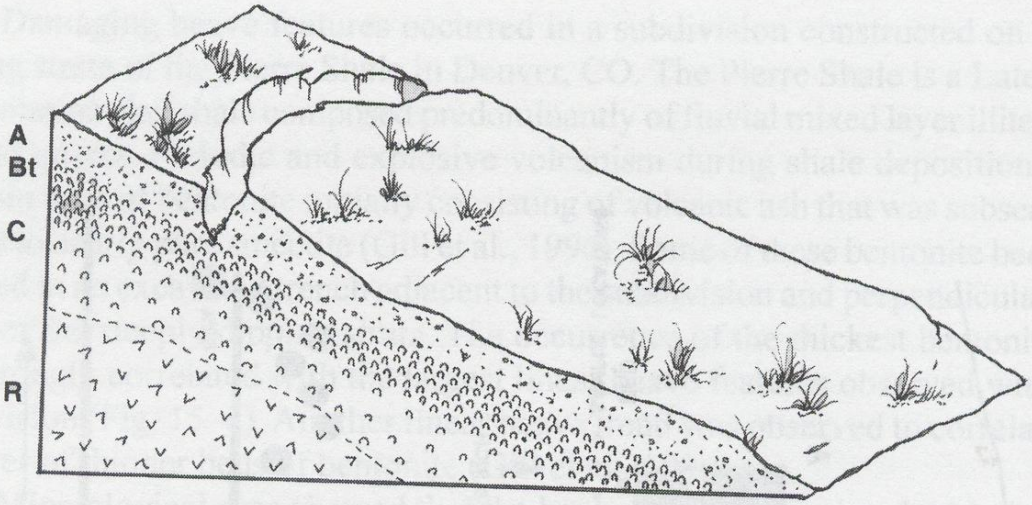

Fig. 15–5. Rotational landslide occurring when water infiltrates through less clayey, more conductive surface horizons (A horizons) into argillic horizons (Bt horizons) containing expansive clays, resulting in a shear zone.

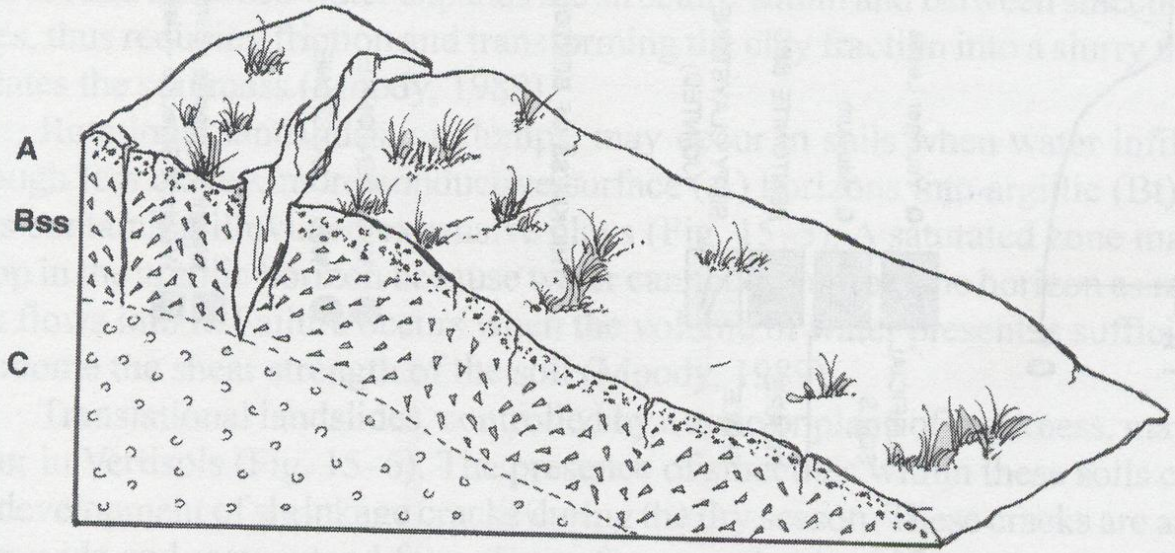

Fig. 15–6. Translational landslide occurring when water infiltrates cracks within a Vertisol. Failure zones occur where cracks in the B horizon (Bss indicates slickensides) end and strong to moderate soil structure becomes weak or massive in the C horizon.

Table 15–2. X-ray diffraction criteria for identification of smectites.

Treatment	Diagnostic d(001) spacings
	nm
Mg-saturated, air-dried	1.4–1.5
Mg-saturated, glycerol liquid	1.7–1.8
Mg-saturated, glycerol vapor	1.5, 1.7–1.8†
K-saturated, air-dried	1.24–1.28
K-saturated, 300°C	0.98–1.01
K-saturated, 550°C	0.98–1.01
Li-saturated, 200– 300°C	0.95, 1.77‡

† Montmorillonite expands to 1.8 nm with glycerol vapor solvation, but beidellite and nontronite do not change in the presence of the vapor and maintain basal spacings of 1.5 nm.

‡ Only montmorillonite collapses in response to Li^+ and heat treatment. Beidellite and nontronite exhibit basal spacings of 1.77 to1.80 nm.

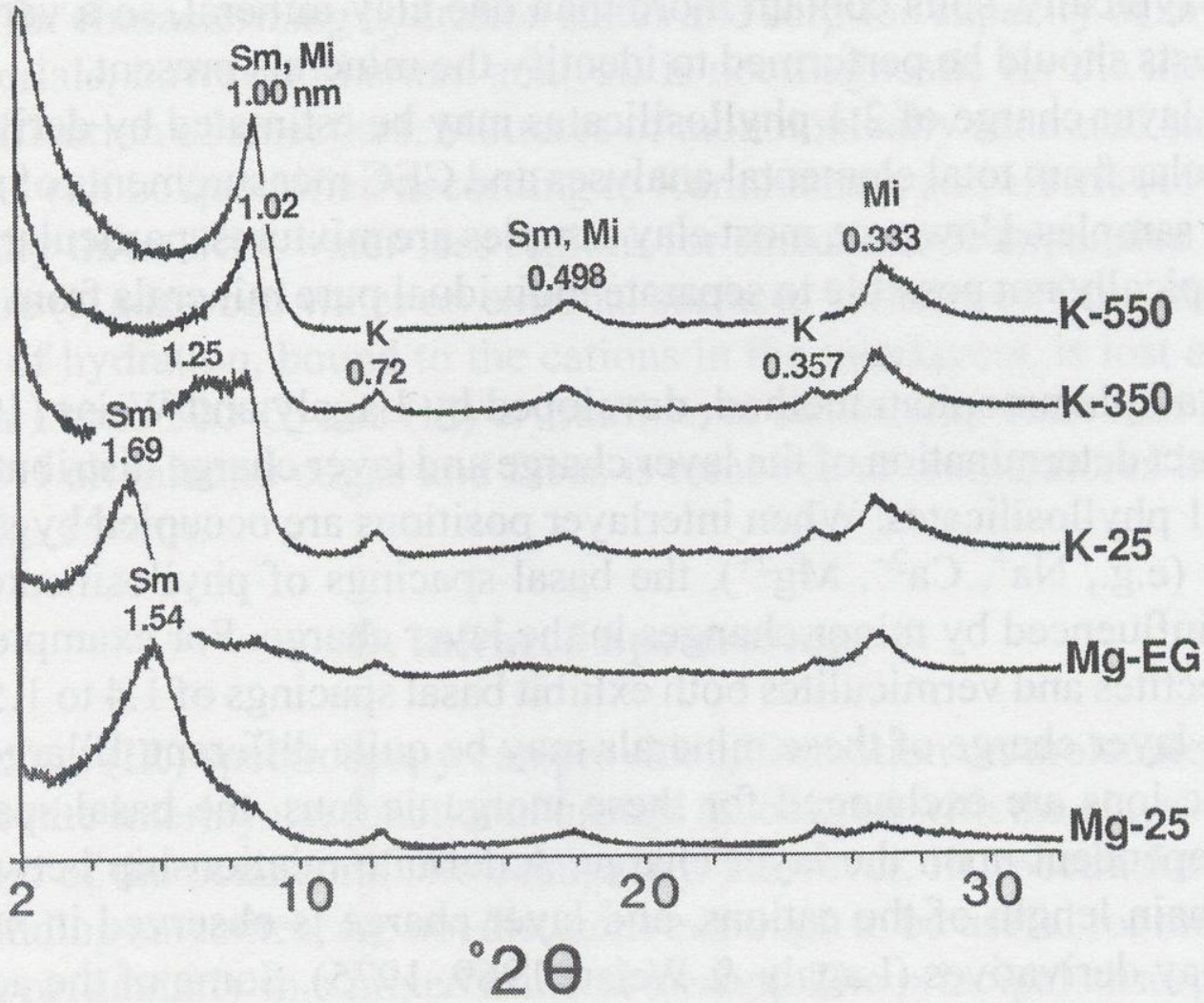

Fig. 15–9. X-ray diffractograms of the fine clay (<0.2 μm) fraction of a Bky2 horizon (135–180 cm) from a fine-loamy, mixed, thermic Typic Haploxeralf after various treatments using Cu Kα radiation. Mg-25 = Mg saturated at room temperature; Mg-EG = Mg-saturated and ethylene glycolated; K-25 = K-saturated at room temperature; K-350 = K-saturated, heated to 350°C for 2 h.; K-550 = K-saturated, heated to 550°C for 2 h. Sm = smectite; Mi = mica (illite); K = kaolinite; Q = quartz.

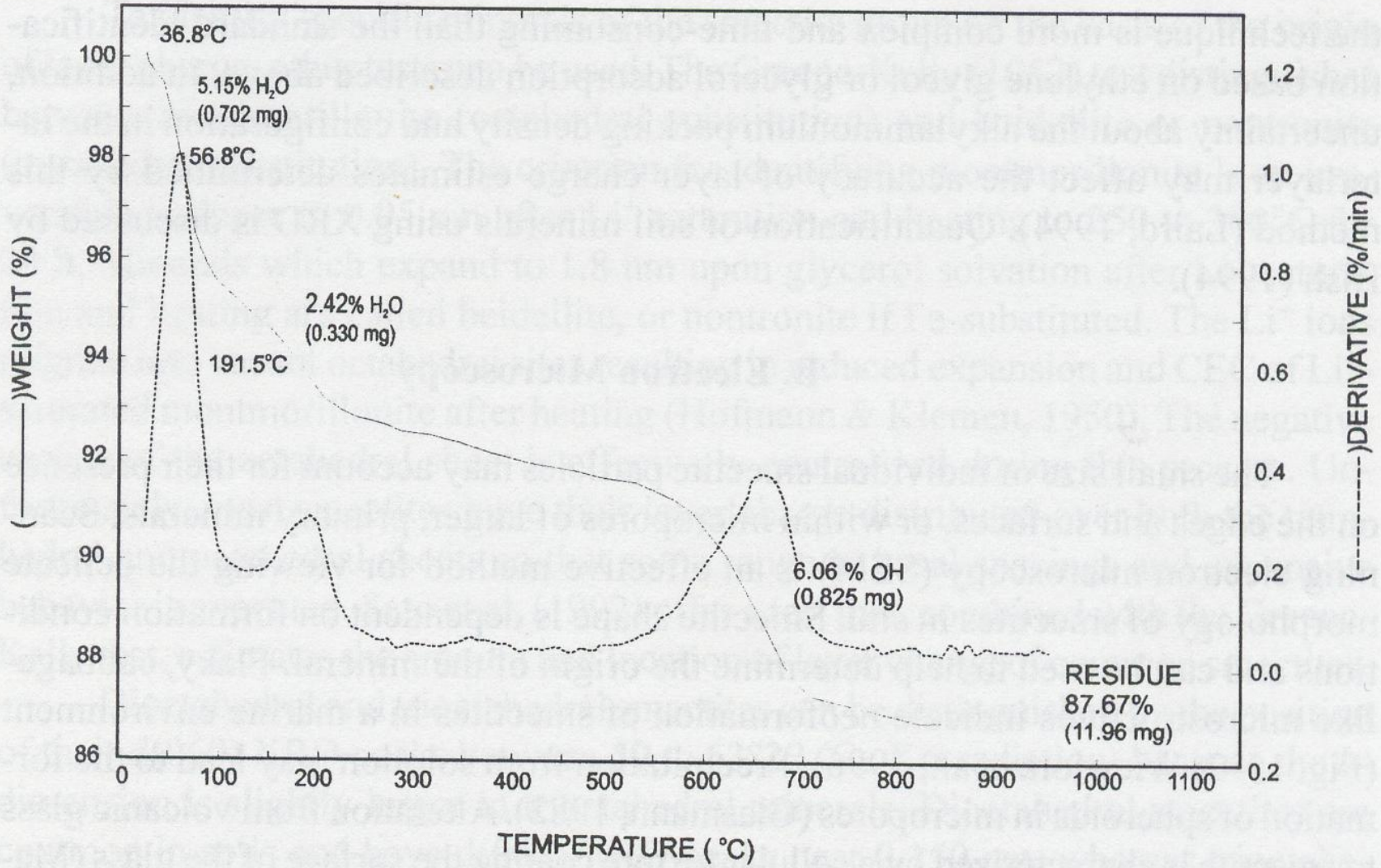

Fig. 15–10. Thermogravimetric analysis curve for smectite SWY-1 (Na-montmorillonite) showing two-stage low-temperature dehydration and dehydroxylation (10°C min^{-1} heating rate, 50 cm^3 min^{-1} N_2 purge, 13.64-mg sample, 0.10–0.35 μm particle size). (Bish & Duffy, 1990; reprinted with permission of the Clay Minerals Society, Boulder, CO).

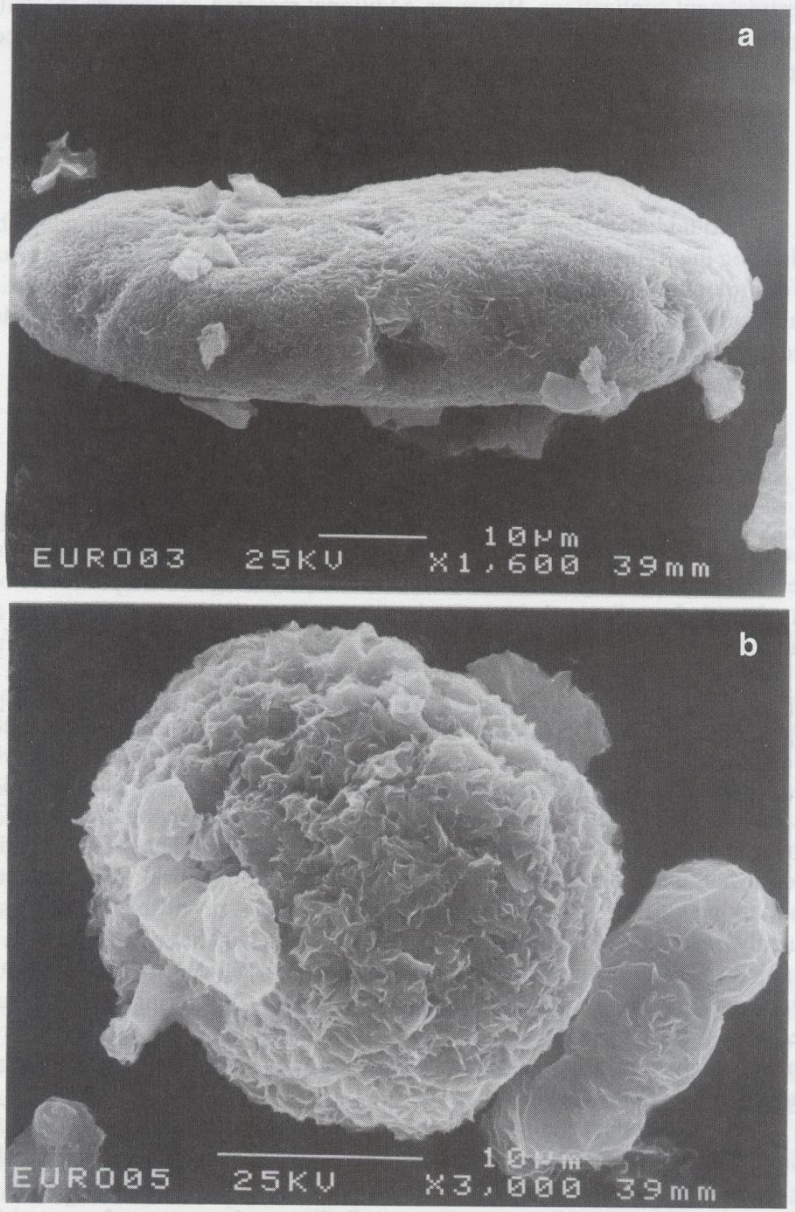

Fig. 15–11.Smectite aggregates from a Spanish bentonite that lacked colloidal properties characteristic of good bentonites (i.e., Atterburg liquid limit of 98% vs. ~400% for model bentonite), yet with a cation exchange of 105 $cmol_c\ kg^{-1}$ similar to model bentonite. Lack of colloidal properties is attributed to 50% silt- and sand-size particles (a) like those shown with edges of the smectite layers shown in rounded particle and (b) characteristic foliar properties of smectite in particle. X-ray diffraction confirmed smectite in silt and sand particles (Courtesy of G.N. White and J.B. Dixon).

Vermiculite

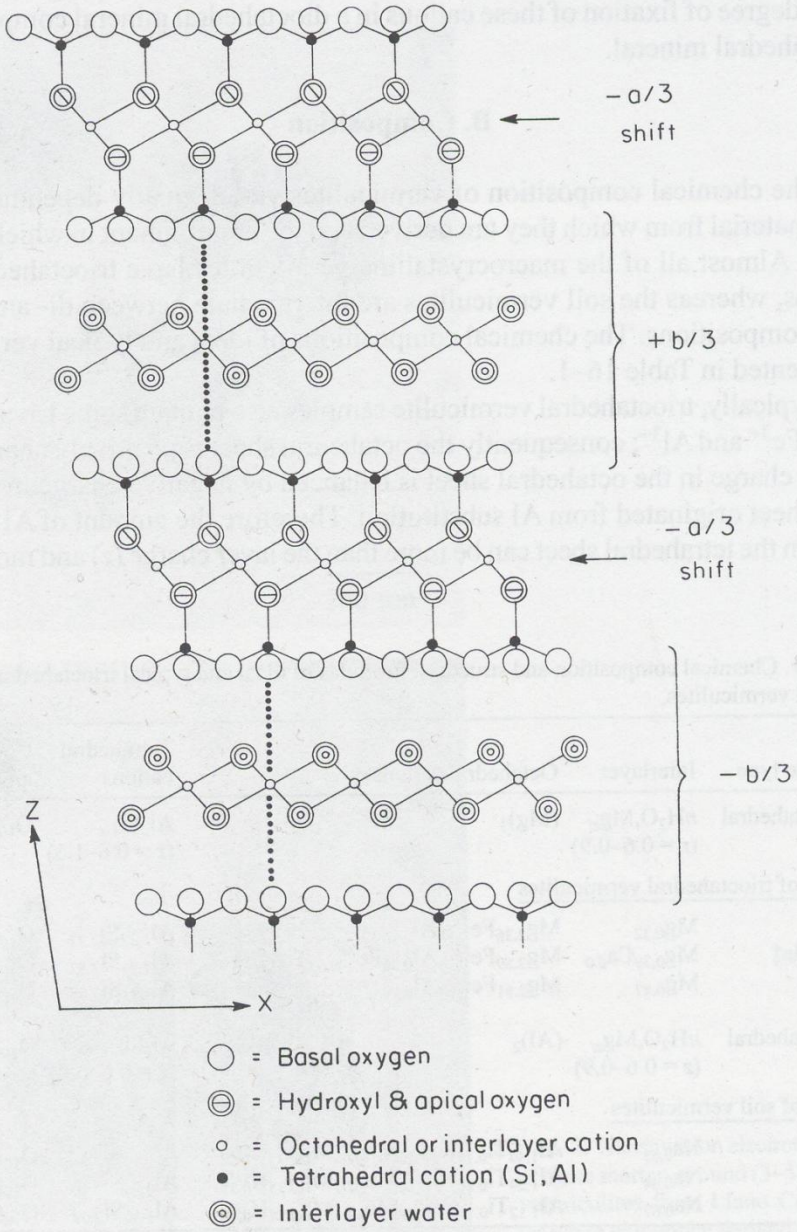

Fig. 16–1. The n[010] view of Llano vermiculite structure, with $-a_1/3$ intralayer shift (L-type) and alternation of $\pm b/3$ shifts between adjacent 2:1 layers. Vertical dots show alignment of interlayer cations between tetrahedra above and below. (Bailey, 1980b).

Table 16–1. Chemical composition and structural formulas of ideal and typical trioctahedral and dioctahedral vermiculites.

Vermiculite type	Interlayer	Octahedral cations	Tetrahedral cations	Coordinating anions
Ideal trioctahedral	$nH_2O,Mg_{z/}$ (z = 0.6–0.9)	$(Mg)_3$	Al_xSi_{4-x} (x = 0.6–1.5)	$O_{10}(OH)_2$
Examples of trioctahedral vermiculites				
Kenya†	$Mg_{0.32}$	$Mg_{2.36}Fe^{3+}_{0.48}Al_{0.16}$	$Al_{1.27}Si_{2.72}$	$O_{10}(OH)_2$
Santa Olalla‡	$Mg_{0.39}Ca_{0.0}$	$Mg_{2.59}Fe^{3+}_{0.24}Al_{0.06}Fe^{2+}{}_{0.03}Ti_{0.08}$	$Al_{1.28}Si_{2.82}$	$O_{10}(OH)_2$
Llano†	$Mg_{0.47}$	$Mg_{2.81}Fe^{3+}_{0.07}Al_{0.11}$	$Al_{1.11}Si_{2.90}$	$O_{10}(OH)_2$
Ideal dioctahedral	$nH_2O,Mg_{z/}$ (z = 0.6–0.9)	$(Al)_2$	Al_xSi_{4-x} (x = 0.6–0.9)	$O_{10}(OH)_2$
Examples of soil vermiculites				
Sample A§	$Na_{0.61}$	$Al_{1.44}Ti_{0.14}Fe^{3+}_{0.16}Mn_{0.05}Mg_{0.27}H_{0.03}$	$Al_{1.10}Si_{2.90}$	$O_{10}(OH)_2$
Sample B§	$Na_{0.64}$	$Al_{1.24}Ti_{0.18}Fe^{3+}_{0.20}Mn_{0.02}Mg_{0.35}H_{0.25}$	$Al_{0.76}Si_{3.24}$	$O_{10}(OH)_2$
Sample C§	$Na_{0.67}$	$Al_{1.12}Ti_{0.16}Fe^{3+}_{0.29}Mn_{0.03}Mg_{0.75}H_{0.19}$	$Al_{1.31}Si_{2.69}$	$O_{10}(OH)_2$

† Brown et al. (1978).
‡ De La Calle & Suquet (1988).
§ Barshad & Kishk (1969).

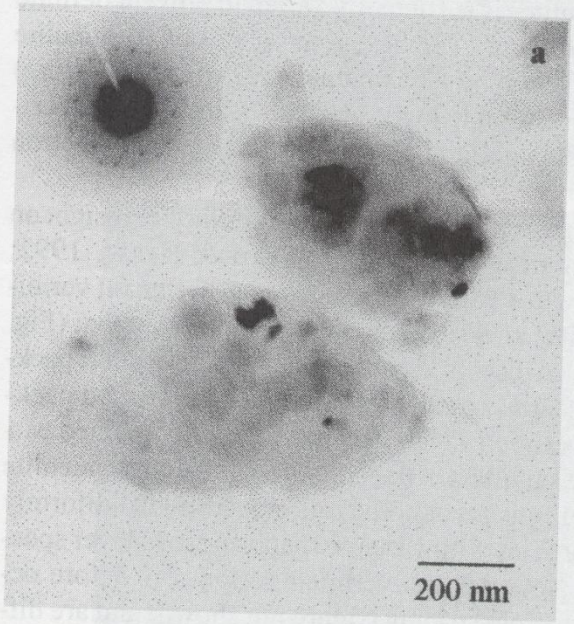

Fig. 16–2. Transmission electron micrographs of agate mortar–ground (3–5 min in water) vermiculites from Llano County, Texas: (a) white phlogopite derived and (b) brown biotite derived. Inserts are selective area diffraction patterns (courtesy of J.B. Dixon).

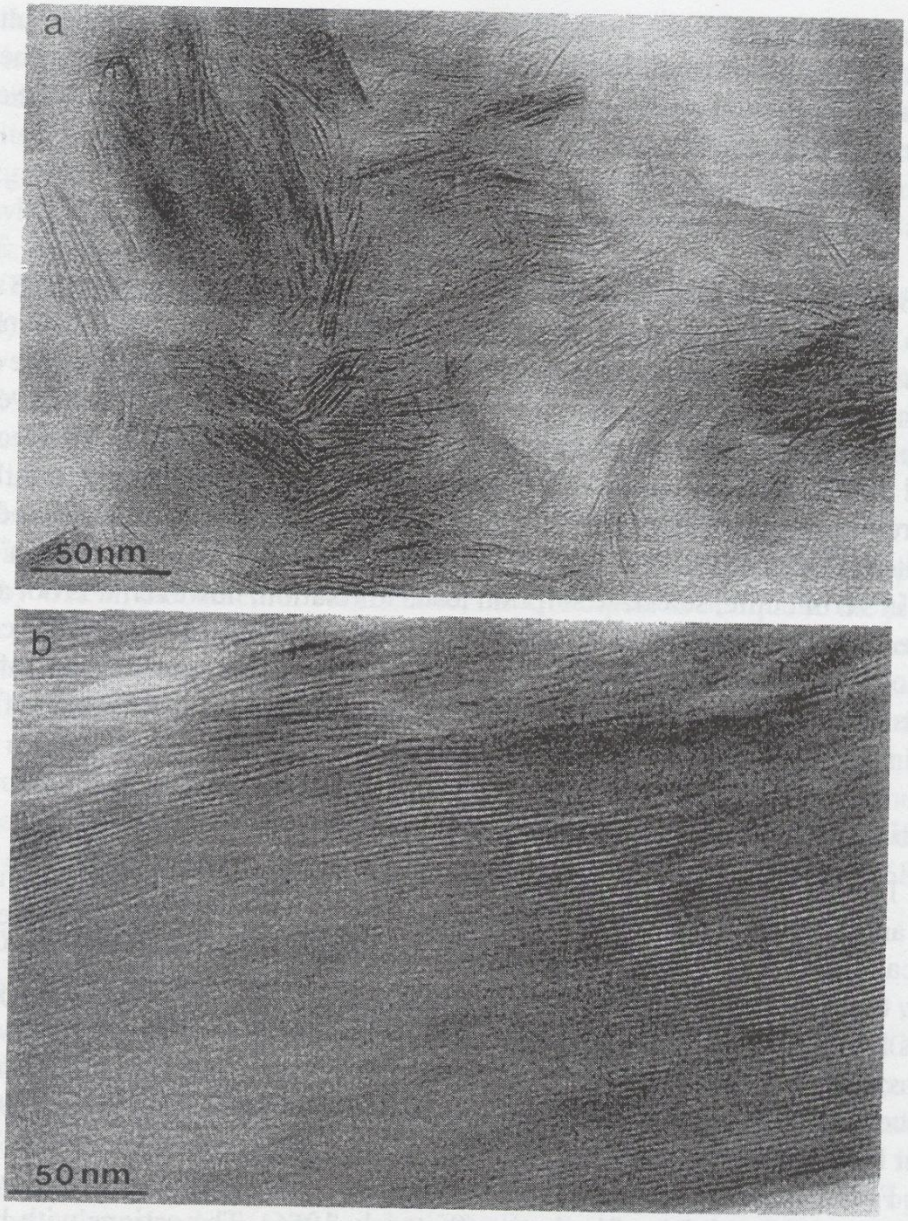

Fig. 16–3. Transmission electron microscopy images after octadecylammonium treatment. (a) extremely fine-grained dispersed particles of Jefferson vermiculite with interlayer spacing varying between 1. 0 and 3.0 nm and (b) Llano vermiculite showing both large crystals with uniformly expanded interlayers and smaller particles with variable shape and interlayer spacing (2.2–2.5 nm spacing) (Vali & Hesse, 1992).

Table 2–2. Hydration energies of common cations.

Ion	Effective ionic radius† (r_{eff})	Ionic potential‡ Z^2/r_{eff}	Enthalpy of hydration§	Hydrolysis constant¶
	nm		kJ mol^{-1}	pK_h
Ca^{2+}	0.126	2.15	−1669	12.7
Mg^{2+}	0.086	2.8	−1998	11.4
K^+	0.165	0.45	−360	
Na^+	0.132	0.5	−444	14.5
Cs^+	0.188	0.4	−315	
Cu^{2+}	0.087	2.6	−2174	7.5
Fe^{3+}	0.069	6.3	−4491	2.2
Fe^{2+}	0.075	2.5	−2009	
Co^{2+}	0.079	2.6	−2106	9.6
Zn^{2+}	0.088	2.6	−2106	9.6
Cd^{2+}	0.124	2.3	−1882	11.7
Pb^{2+}	0.143	2	−1556	7.8
Al^{3+}	0.067	6.9	−4774	5.1
Li^+	0.090	0.7	−559	13.8

† Shannon (1976).
‡ Huheey (1974).
§ Friedman and Krishnan (1973).
¶ Yatsimirksii and Vasil'ev (1960).

Table 16–2. Name and structural formula of commonly used organic cations on the exchange complex of smectite or vermiculite.

Name	Abbreviation	Structure
Dioctadecyldimethylammonium	$DODMA^+$	CH_3 | CH_3-N^+-$(CH_2)_{17}$-CH_3 | $(CH_2)_{17}$-CH_3)
Hexadecyltrimethylammonium	$HDTMA^+$	CH_3 | CH_3-N^+-$(CH_2)_{15}$-CH_3 | CH_3
Hexadecylpyridinium	$HDPY^+$	N^+-$(CH_2)_{15}$-CH_3
Trimethylphenylammonium	$TMPA^+$	CH_3 | CH_3 -N^+-  | CH_3
Tetramethylammonium	TMA^+	CH_3 | CH_3 -N^+-CH_3 | CH_3
Decylammonium	C10	$CH_3(CH_2)_9NH_3^+$
Dodecylammonium	C12	$CH_3(CH_2)_{11}NH_3^+$

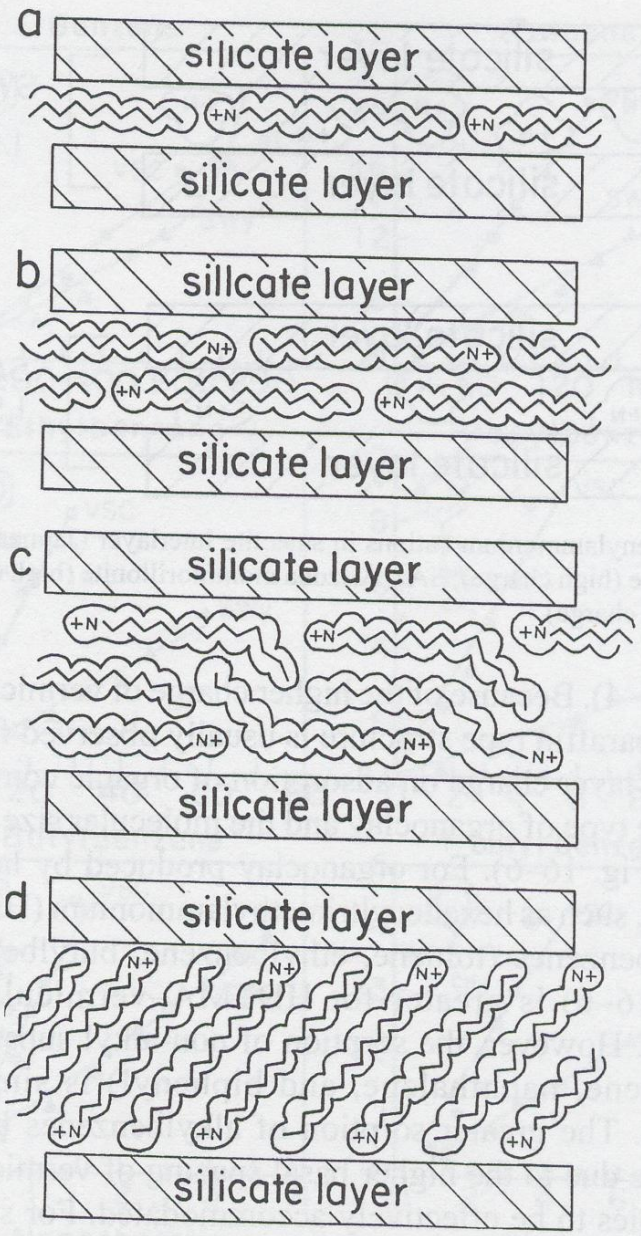

Fig. 16–4. Alkylammonium expansion of an expandable clay mineral: (a) monolayer (1.37 nm), (b) bilayer (1.77 nm), (c) pseudotrimolecular layer (2.17 nm), and (d) paraffin complex (>2.2 nm). (Jaynes & Boyd, 1991a).

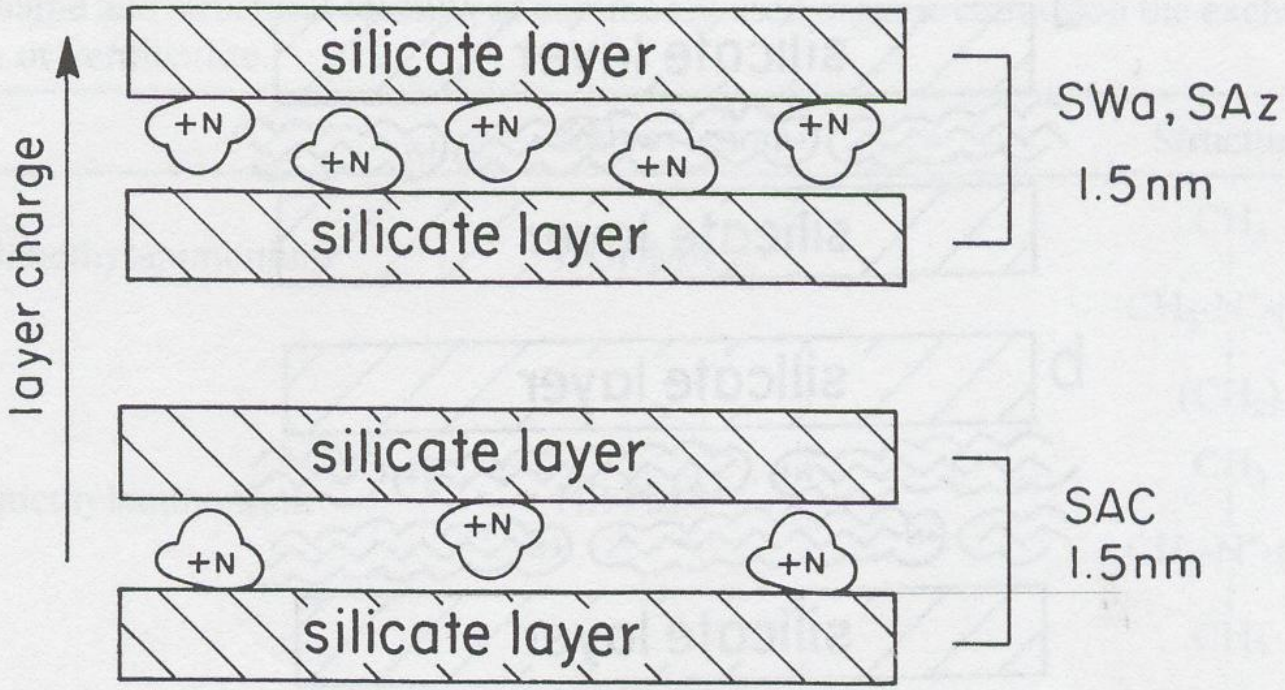

Fig. 16–5. Trimethylphenylammonium cations in smectite interlayer (Jaynes & Boyd, 1991b). SWa, Washington nontronite (high charge); SAz, Arizona montmorillonite (high charge); SAC, Wyoming montmorillonite (low charge).

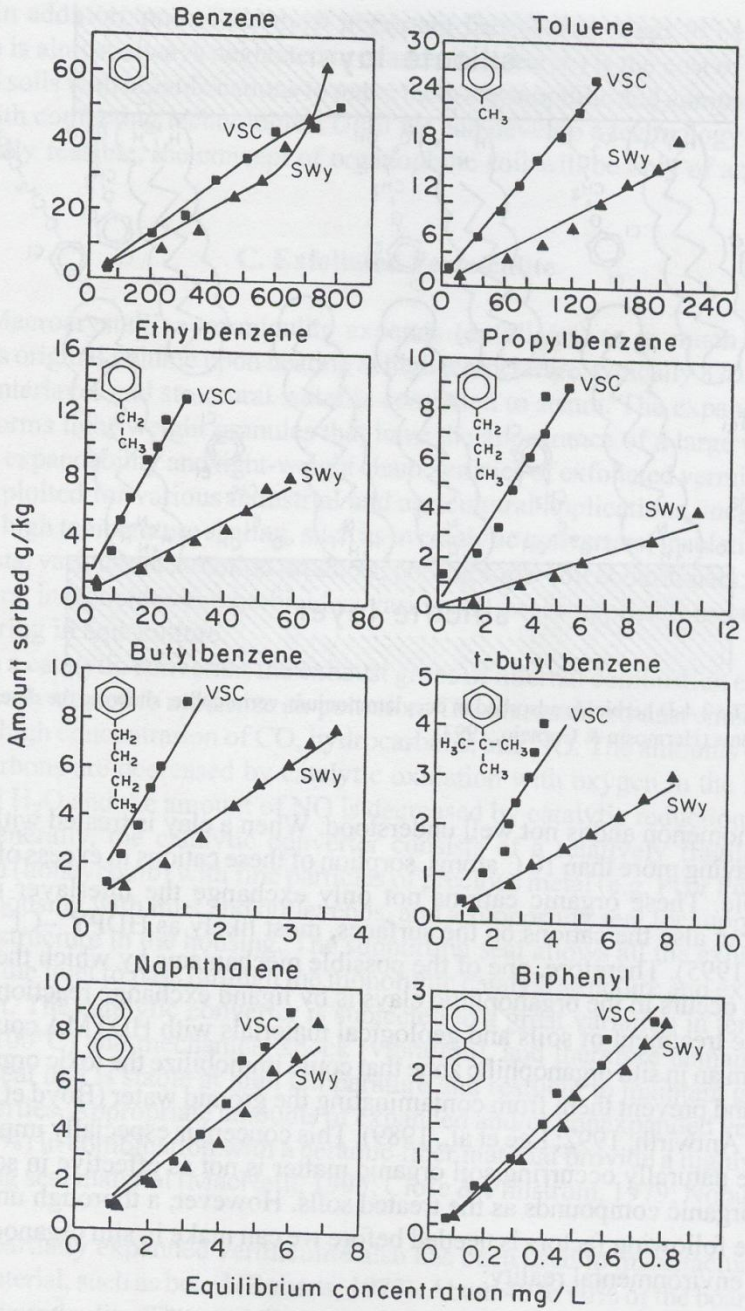

Fig. 16–6. Sorption of the organic compounds benzene, toulene, ethylbenzene, propylbenzene, butylbenzene, *t*-butylbenzene, napthalene, and biphenyl on HDTMA-VSC (South Carolina vermiculite) and HDTMA-SWy-1 (Wyoming montmorillonite). (Jaynes & Boyd, 1991a).